A non-iterative partitioned computational method with the energy conservation property for time-variant dynamic systems

Peng Yuan[a], Ka-Veng Yuen[b]*, Michael Beer[acd], C.S. Cai[e], Wangji Yan[b]

[a] Institute for Risk and Reliability, Leibniz Universität Hannover, Callinstr. 34, 30167 Hannover, Germany

[b] State Key Laboratory of Internet of Things for Smart City and Department of Civil and Environmental Engineering, University of Macau, PR China

[c] Institute for Risk and Uncertainty and School of Engineering, University of Liverpool, Peach Street, Liverpool L69 7ZF, UK

[d] International Joint Research Center for Engineering Reliability and Stochastic Mechanics, Tongji University, 1239 Siping Road, Shanghai 200092, PR China

[e] Department of Bridge Engineering, Southeast University, Nanjing 211189, China

Peng Yuan [a*], E-mail: peng.yuan@irz.uni-hannover.de

Ka-Veng Yuen [b]*, E-mail: kvyuen@um.edu.mo (Corresponding author)

Michael Beer [acd], E-mail: beer@irz.uni-hannover.de

C.S. Cai [e], E-mail: cscai@seu.edu.cn

Wangji Yan[b], E-mail: wangjiyan@um.edu.mo

Abstract: A non-iterative partitioned computational method with the energy conservation property is proposed in this study for calculating a large class of time-variant dynamic systems comprising multiple subsystems. The velocity continuity conditions are first assumed in all interfaces of the partitioned subsystems to resolve the interface link forces. The Newmark integration scheme is subsequently employed to independently calculate the responses of each system based on the obtained link forces. The proposed method is thus divided into two computational modules: multi-partitioned structural analyzers and an interface solver, providing a modular solution for time-variant systems. The proposed method resolves the long-standing problem of iterative computation required in partitioned time-variant systems. More specifically, the proposed method eliminates the need for time-variant matrix formation and the utilization of complex iterative procedures in partitioned computations, which significantly improves the computational efficiency. The derivation process and theoretical demonstration of the proposed method are thoroughly presented through a representative example, i.e., a vehicle-rail-sleeper-ballast time-variant system. The proposed method's accuracy, energy conservation property, and efficiency are systematically demonstrated in comparison with the results of the global model, highlighting its superior performance. A more general example provided in Appendix C demonstrates that the proposed method is not confined to the analysis of vehicle-rail-sleeper-ballast systems but is applicable to other structural dynamic systems.

Keywords: Time-variant systems; Partitioned computation; Vehicle-bridge interaction; Energy conservation; Stability and accuracy

1 Introduction

The design, modeling, and analysis of large and complex dynamic systems are often impracticable/time-consuming via monolithic models due to physical property differences in different computational domains [1–4]. Partitioned computation offers a promising solution, where each system is independently designed and analyzed [5–7], and different computational methods, such as efficient explicit integration methods or unconditionally stable implicit integration methods [8,9], are designated in different computational domains/subsystems based on the physical properties of subsystems. Thus, partitioned computational methods remarkably improved the computational efficiency and accuracy of large and complex dynamic systems.

Partitioned computation methods are typically applied to time-invariant dynamic systems consisting of two subsystems. Consequently, a multi-physics analysis dealing with interactions among multiple subsystems (≥ 3) presents a new challenge. Moreover, when there is a physical relative motion between the interconnected subsystems, the interface coupling between them becomes a more crucial concern. Typical examples of time-variant systems arise in dynamic contact problems, where relative moving velocity exists among the interconnected subsystems, such as the vehicle-bridge interaction system [10–12] and systems involving sliding friction interfaces [13–16]. These challenges emerging in time-variant dynamic systems demand not only modular simulation capabilities for each subsystem but also, more critically, the maximum possible separation of interface problems in individual subsystems [17]. Two fundamental approaches can be identified for solving multi-subsystem problems: monolithic schemes [18–23] and partitioned schemes [24–28].

Monolithic schemes. In a monolithic coupling system, all individual physical subsystems, including their interactions, are solved in global system equations with consistent discretization and integration schemes. Highly robust and accurate simulations of large and complex problems are often achieved by solving global systems. However, this comes at the cost of the flexibility of the monolithic approach as it requires the solver to be customized for the specific application and lacks easy modifiability. Furthermore, modifying the coupling problem requires substantial effort and significantly prolongs the method and software development time [2]. For instance, in time-variant systems, such as the time-variant vehicle-bridge global system caused by vehicle motion, the large global system matrix necessitates reassembly and recalculation at each time step, consuming significant computational resources [27]. Moreover, by employing condensation techniques that eliminate the degrees of freedom (DOFs) of the vehicle, Yang and Yau [18,21–23] first transformed the vehicle equations into equivalent stiffness equations and subsequently condensed them into the bridge system. Due to the time-variant contact point, the system matrix in [18,21–23] typically varies over time, necessitating updating and factorization of the matrix at every time step, resulting in significant computational overhead for stochastic calculations. In addition, Ge [29] introduced a time-parameter freezing technique to transform the linear time-varying vehicle-bridge interaction problem into a sequence of linear time-invariant problems.

Partitioned schemes. In contrast to the monolithic method, partitioned computational methods usually employ independent solvers for different subsystems, such as explicit/implicit solvers. The exchange of physical information between solvers is limited to the coupling interfaces [8]. Each physical subsystem can be designed as an independent system and be solved by using tailored discretization and integration schemes. This approach offers enhanced flexibility for the overall coupling problem. For example, Xia et al. [24,25] proposed a loosely coupled iterative algorithm that computes the vehicle and bridge subsystems separately using contact forces obtained through iterations. Xia's iterative algorithm was subsequently optimized in a recent study [26–28]. Stoura et al. [30] introduced auxiliary contact bodies between the vehicle and bridge systems for conducting iterative analysis based on predefined convergence criteria. Kalaycıoğlu [31] proposed a decoupling Method for the dynamic decoupling problem of nonlinear structures, while this method is applicable only if the nonlinearity can be modeled as a single nonlinear element. Existing partitioned methods require an iterative procedure based on predefined convergence criteria at each time step. However, conducting a single calculation is already highly time-consuming for large and complex systems. The success of the calculation relies directly on the chosen convergence criterion, and developing convergence criteria for complex time-variant systems poses significant challenges. Furthermore, for partitioned systems with multiple interfaces, convergence criteria must be defined for each interface, and achieving simultaneous convergence at multiple interfaces is challenging. Convergence calculations for time-variant interfaces are even more complex and time-consuming. Moreover, even if the calculation results converge and approximate well the true values, determining if there is dissipation of system energy or if certain response frequencies are being filtered remains difficult.

These above challenges emerging in time-variant dynamic systems, e.g., the limitation of the number of subsystems, the requirement of iterative procedures, and the determination of the convergence criterion at multiple interfaces, motivate us to investigate a formulation that enables modular computational modeling and deals with multi-subsystems interface problems in time-variant systems. A general, simply-structured, and efficient method, i.e., a non-iterative partitioned computational method with the energy conservation property, is proposed in this study for solving a large class of time-variant dynamic systems. The proposed method resolves the long-standing problem of iterative computation required in partitioned time-variant systems. The time-variant matrix formation and the utilization of complex iterative procedures are not required in partitioned computations, which significantly improves computational efficiency. To provide a clear illustration of the proposed method, the remaining sections of this study are organized as follows. A typical **v**ehicle-**r**ail-sleeper-**b**allast **s**ystem (VRBS) divided into five subsystems, serving as an illustrative example, is established in Section 2. The non-iterative partitioned computational method for time-variant dynamic systems is proposed in Section 3. The stability of the proposed method is investigated in Section 4 through the system energy property. The proposed method's properties, including stability, computational accuracy, and efficiency, are numerically discussed in Section 5 via the built VRBS including the five/two-subsystem models.

2 Establishment of the partitioned VRBS equations

To demonstrate the derivation process of the proposed method in detail, a simplified VRBS, as an illustrative example, is partitioned into five subsystems according to their properties. The interface continuity conditions between the interconnected subsystems serve as supplementary conditions for calculating the interface link forces. It is important to emphasize that the proposed method is applicable to partitioned solutions of other time-variant dynamic systems as well. Fewer or more system-partitioned solutions can be derived similarly, as demonstrated in subsequent sections.

2.1 *Modeling of the vehicle subsystem*

The 2D vehicle model, as shown in Fig. 1, is adopted to illustrate the proposed method in this study. Three assumptions are made in modelling the vehicle. Specifically, (1) the vehicle maintains a constant speed; (2) each vehicle consists of seven rigid bodies (i.e., one car body, two bogies, and four wheelsets), which are interconnected by the primary and secondary suspension systems with linear springs and dampers; and (3) the DOFs for the car body, two bogies, and four wheelsets are denoted as (z_c, β_c), (z_{t1}, β_{t1}), (z_{t2}, β_{t2}), and (z_{w1}, z_{w2}, z_{w3}, z_{w4}), respectively, as marked in Fig. 1. These DOFs collectively form the vehicle vector $\boldsymbol{U}_V = [z_c, \beta_c, z_{t1}, \beta_{t1}, z_{t2}, \beta_{t2}, z_{w1}, z_{w2}, z_{w3}, z_{w4}]^T$. To establish the equation of motion, a force analysis for the seven rigid bodies is carried out, as shown in Fig. 2. The derivation for Eq. (1) is provided in Appendix A, and the incremental form of the vehicle governing equation is presented as follows:

$$\mathbf{M}_V\Delta\ddot{\mathbf{U}}_{(V,t_{i+1})}+\mathbf{C}_V\Delta\dot{\mathbf{U}}_{(V,t_{i+1})}+\mathbf{K}_V\Delta\mathbf{U}_{(V,t_{i+1})}+\left(\boldsymbol{L}_1^{W\cdot R}\right)^T\Delta\boldsymbol{P}_{(VR,t_{i+1})}=\Delta\mathbf{P}_{VE}+\Delta\mathbf{Fv} \quad (1a)$$

$$\Delta\mathbf{Fv}=\left(\boldsymbol{L}_1^{W\cdot R}\right)^T\left(\boldsymbol{L}_{1t_{i+1}}^{R\cdot W}-\boldsymbol{L}_{1t_i}^{R\cdot W}\right)\mathbf{U}_{(R,t_i)}k_0+\left(\boldsymbol{L}_1^{W\cdot R}\right)^T\left(\boldsymbol{L}_{1t_{i+1}}^{R\cdot W}-\boldsymbol{L}_{1t_i}^{R\cdot W}\right)\dot{\mathbf{U}}_{(R,t_i)}c_0 \quad (1b)$$

where $\mathbf{M}_V$, $\mathbf{C}_V$, and $\mathbf{K}_V$ are the mass matrix, damping matrix, and stiffness matrix of the vehicle, respectively; the linearized Hertzian spring (k_0 = 23382063.67) and damping (c_0), as marked in Fig. 1 (c), are employed to simplify and simulate the wheel-rail connection forces; $\Delta\mathbf{P}_{VR} \in \mathbb{R}^{L_V}$, $\Delta\mathbf{P}_{VE} \in \mathbb{R}^{L_V}$, and $\Delta\mathbf{F}_V \in \mathbb{R}^{L_V}$ refer to the link-force increment between interconnected subsystems (where L_V is the number of DOFs of the wheelsets), the external force increment, and the time-variant loadings caused by the vehicle running, respectively; $\Delta\dot{\mathbf{U}}_V$ and $\Delta\ddot{\mathbf{U}}_V$ are, respectively, the velocity and acceleration increments at a time step; and all increments are calculated within a time step Δh from t_i to t_{i+1} such as $\Delta\dot{\boldsymbol{U}}_{(V,\ t_{i+1})} = \dot{\boldsymbol{U}}_{(V,\ t_{i+1})} - \dot{\boldsymbol{U}}_{(V,\ t_i)}$. The subscript (i.e., V = Vehicle, R = Rail, S = Sleeper, B = Ballast, Br = Bridge) is employed here to distinguish matrix and vector types of different subsystems (similarly hereinafter). In addition, $\boldsymbol{L}_1^{W\cdot R}$ is a Boolean matrix, where the subscript and superscripts denote interface numbers and two subsystem symbols, respectively. The order of letters in the superscripts determines the type of Boolean matrix. For instance, the matrix $\boldsymbol{L}_1^{W\cdot R}$ with $L_V \times N_V$ dimensions is the Boolean matrix of the first interface on the **w**heel side, where N_V represents the number of the vehicle subsystem's DOFs. It is important to note that all cases discussed in the study are linear scenarios of subsystems connected with springs, and the nonlinear cases will be further studied in further work. In addition, the moving vehicle results in time-variant rail-wheelset contact points, making the Boolean matrix of the first interface on the **r**ail side (i.e., $\boldsymbol{L}_{1t_{i+1}}^{R\cdot W}$) also time-variant. More detailed information on the Boolean matrix can be found in [32–34].

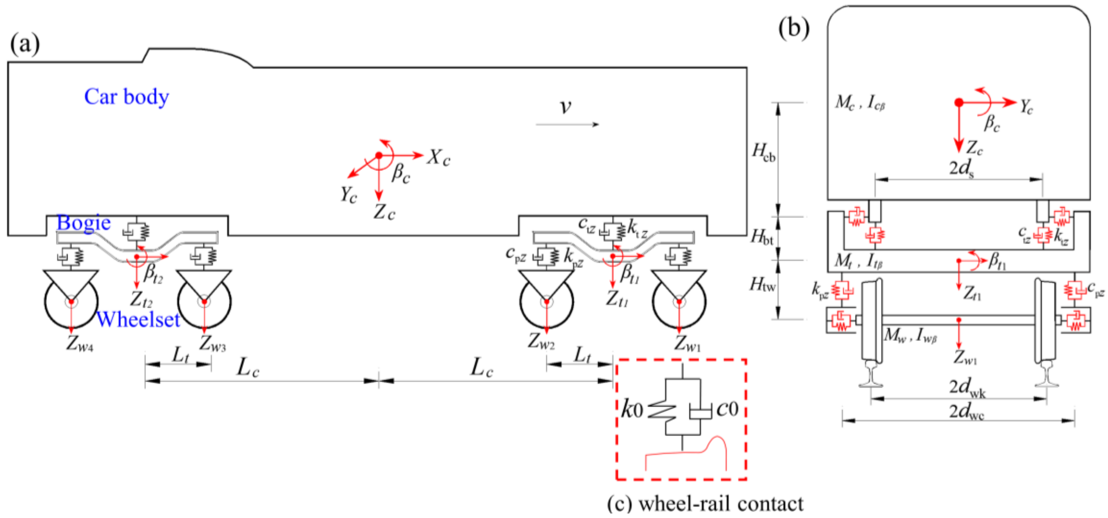

Fig. 1 The 2D vehicle model. (a) Lateral view, (b) back view, and (c) wheel-rail contact information. Note that the notations (k_{tz}, c_{tz}) and (k_{pz}, c_{pz}) denote the vertical stiffness and damping of the primary and secondary suspension systems, respectively. The symbols (M_c, $I_{c\beta}$), (M_t, $I_{t\beta}$), and (M_w, $I_{w\beta}$) are the mass and moment of inertia of the car body, bogie, and wheelsets, respectively. (L_t, L_c) and (H_{tw}, H_{bt}, and H_{cb}) are, respectively, horizontal and vertical distances of the designated rigid body centers.

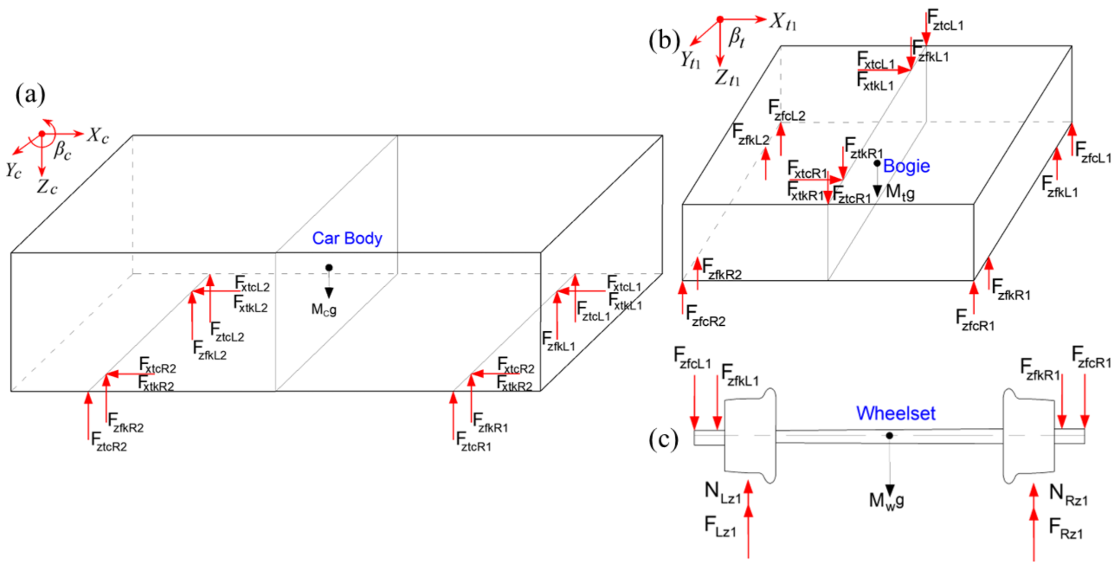

Fig. 2 Schematic diagram of the vehicle force analysis. (a) Car body, (b) the first bogie, and (c) the first wheelsets. The subscripts under the symbol **F** represent four components: directions (x and z), positions (f and t), types (c and k), and orientations (L and R) of the applied forces. For instance, $\mathrm{F}_{\mathrm{xtcL1}}$ denotes the damping force (c) of the secondary suspension system (t) along the x direction at the left side (L) of the car body.

2.2 *Modeling of the rail-bridge subsystems*

The rail subsystem plays a crucial role in distributing and attenuating high-frequency loadings between the wheels and the rail. Considering the universality, the ballasted rail system shown in Fig. 3(a) is built in this study. To derive the governing equations of their respective subsystems, the force analysis for the rail, sleeper, ballast, and bridge is performed, as depicted in Figs. 3(b) and (c). The incremental forms of these governing equations are presented below:

$$\begin{aligned}&\mathbf{M}_R\Delta\ddot{\mathbf{U}}_{(R,t_{i+1})}+\mathbf{C}_R\Delta\dot{\mathbf{U}}_{(R,t_{i+1})}+\mathbf{K}_R\Delta\mathbf{U}_{(R,t_{i+1})}\\&+\left(\boldsymbol{L}_{1t_{i+1}}^{R\cdot W}\right)^T\Delta\boldsymbol{P}_{(VR,t_{i+1})}+\left(\boldsymbol{L}_2^{R\cdot S}\right)^T\Delta\mathbf{P}_{(RS,t_{i+1})}=\Delta\mathbf{P}_{RE}+\Delta\mathbf{Fr}\end{aligned}\tag{2a}$$

$$\begin{aligned}\Delta\mathbf{Fr}=&-\left(\boldsymbol{L}_{1t_i}^{R\cdot W}\right)^T\left(\boldsymbol{L}_{1t_i}^{R\cdot W}\mathbf{U}_{(R,t_i)}-\boldsymbol{L}_0^{W\cdot R}\mathbf{U}_{(V,t_i)}\right)k_0+\left(\boldsymbol{L}_{1t_{i+1}}^{R\cdot W}\right)^T\left(\boldsymbol{L}_0^{W\cdot R}\mathbf{U}_{(V,t_i)}-\boldsymbol{L}_{1t_{i+1}}^{R\cdot W}\mathbf{U}_{(R,t_i)}\right)k_0\\&-\left(\boldsymbol{L}_{1t_i}^{R\cdot W}\right)^T\left(\boldsymbol{L}_{1t_i}^{R\cdot W}\dot{\mathbf{U}}_{(R,t_i)}-\boldsymbol{L}_0^{W\cdot R}\dot{\mathbf{U}}_{(V,t_i)}\right)c_0+\left(\boldsymbol{L}_{1t_{i+1}}^{R\cdot W}\right)^T\left(\boldsymbol{L}_0^{W\cdot R}\dot{\mathbf{U}}_{(V,t_i)}-\boldsymbol{L}_{1t_{i+1}}^{R\cdot W}\dot{\mathbf{U}}_{(R,t_i)}\right)c_0\end{aligned}\tag{2b}$$

$$\mathbf{M}_S\Delta\ddot{\mathbf{U}}_{(S,t_{i+1})}+\mathbf{C}_S\Delta\dot{\mathbf{U}}_{(S,t_{i+1})}+\mathbf{K}_S\Delta\mathbf{U}_{(S,t_{i+1})}+\left(\left(\boldsymbol{L}_2^{S\cdot R}\right)^T\Delta\mathbf{P}_{(RS,t_{i+1})}+\left(\boldsymbol{L}_3^{S\cdot B}\right)^T\Delta\mathbf{P}_{(SB,t_{i+1})}\right)=\Delta\mathbf{P}_{SE}\tag{3}$$

$$\mathbf{M}_B\Delta\ddot{\mathbf{U}}_{(B,t_{i+1})}+\mathbf{C}_B\Delta\dot{\mathbf{U}}_{(B,t_{i+1})}+\mathbf{K}_B\Delta\mathbf{U}_{(B,t_{i+1})}+\left(\left(\boldsymbol{L}_3^{B\cdot S}\right)^T\Delta\mathbf{P}_{(SB,t_{i+1})}+\left(\boldsymbol{L}_4^{B\cdot Br}\right)^T\Delta\mathbf{P}_{(BBr,t_{i+1})}\right)=\Delta\mathbf{P}_{BE}\tag{4}$$

$$\mathbf{M}_{Br}\Delta\ddot{\mathbf{U}}_{(Br,t_{i+1})}+\mathbf{C}_{Br}\Delta\dot{\mathbf{U}}_{(Br,t_{i+1})}+\mathbf{K}_{Br}\Delta\mathbf{U}_{(Br,t_{i+1})}+\left(\boldsymbol{L}_4^{Br\cdot B}\right)^T\Delta\mathbf{P}_{(BBr,t_{i+1})}=\Delta\mathbf{P}_{BrE}\tag{5}$$

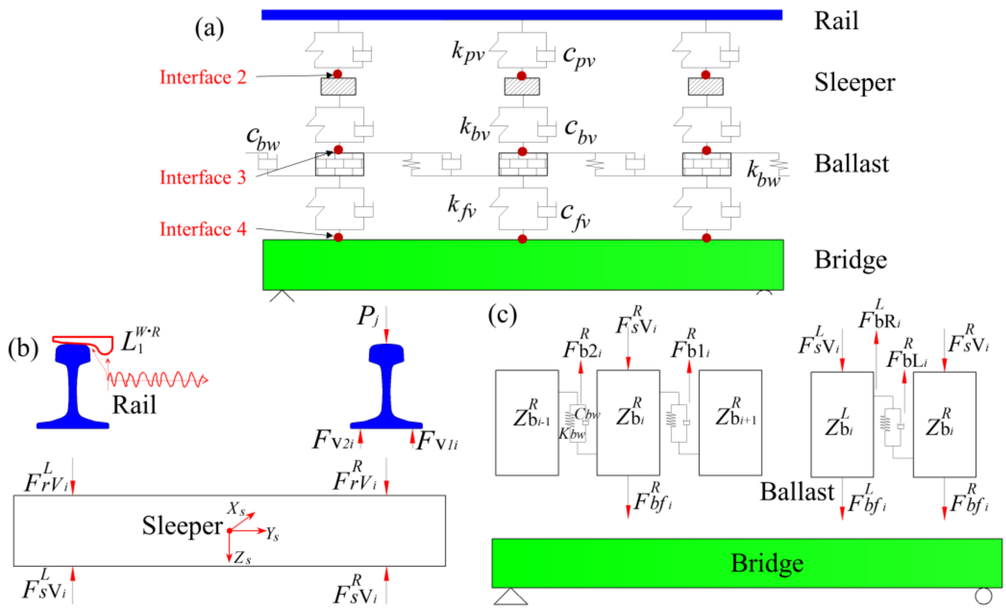

Fig. 3 Schematic diagram of the force analysis of the rail-sleeper-ballast-bridge subsystem. (a) Rail-sleeper-ballast-bridge subsystem, (b) the force analysis of the rail-sleeper subsystem, and (c) the force analysis of the ballast-bridge subsystem. Note that the notations (k_p, c_p), (k_b, c_b), and (k_f, c_f) denote the vertical stiffness and damping of the rail, sleeper, and ballast, respectively. The superscript $\boldsymbol{F}$ represents the force orientation (L = Left), and the first and second subscripts under $\boldsymbol{F}$ represent the name of the subsystem (r = rail) and the vertical force number, respectively.

The detailed derivation process of Eqs. (2) to (5) is given in Appendix A. The five subsystems are interconnected by the four link forces (i.e., $\Delta\mathbf{P}_{VR}$, $\Delta\mathbf{P}_{VS}$, $\Delta\mathbf{P}_{SB}$, and $\Delta\mathbf{P}_{B.Br}$). Note that DOFs of all interfaces must be compatible [35]. If the values of all link forces (i.e., the unknown quantities) are given in advance, all subsystems will be decoupled into independent subsystems and computed independently using their respective integration schemes. The interface continuity conditions between subsystems are thus explored to compute the link forces in the next section.

2.3 *Interface continuity conditions*

To calculate the link forces and ensure the interface continuity of all kinematic quantities, the velocity continuity conditions are selected and imposed on the corresponding interfaces [5,33,36], as shown in Figs. 3(b) and 4. Note that the displacement/acceleration continuity conditions may cause the system energy dissipation gradually, namely, the partitioned system is not stable. Further discussion on these two continuity conditions will be investigated in future study. The four-velocity continuity conditions are expressed as follows:

$$\boldsymbol{L}_1^{W\cdot R}\Delta\dot{\boldsymbol{U}}_{(V,t_{i+1})}+\boldsymbol{L}_{1t_{i+1}}^{R\cdot W}\Delta\dot{\boldsymbol{U}}_{(R,t_{i+1})}=0 \tag{6}$$

$$\boldsymbol{L}_2^{R\cdot S}\Delta\dot{\boldsymbol{U}}_{(R,t_{i+1})}+\boldsymbol{L}_2^{S\cdot R}\Delta\dot{\boldsymbol{U}}_{(S,t_{i+1})}=0 \tag{7}$$

$$\boldsymbol{L}_3^{S\cdot B}\Delta\dot{\boldsymbol{U}}_{(S,t_{i+1})}+\boldsymbol{L}_3^{B\cdot S}\Delta\dot{\boldsymbol{U}}_{(B,t_{i+1})}=0 \tag{8}$$

$$\boldsymbol{L}_4^{B\cdot Br}\Delta\dot{\boldsymbol{U}}_{(B,t_{i+1})}+\boldsymbol{L}_4^{Br\cdot B}\Delta\dot{\boldsymbol{U}}_{(Br,t_{i+1})}=0 \tag{9}$$

Due to the vehicle running, the Boolean matrix of the first interface on the rail side (i.e., $\boldsymbol{L}_{1t_{i+1}}^{R\cdot W}$) is time-varying. In other words, the velocity continuity condition in the first interface, as shown in Eq. (6), is time-varying while the remaining conditions remain time-invariant. At this point, the four-velocity continuity conditions (See Eqs. (6) ~ (9)) are assumed to solve the four-link forces (See Fig. 4). Building upon the velocity conditions, a novel method is proposed to determine the link forces and decouple and solve VRBS in the next sections. The proposed method consists of multi-partitioned structural analyzers and an interface solver, which will be demonstrated from the perspectives of theoretical and numerical analysis.

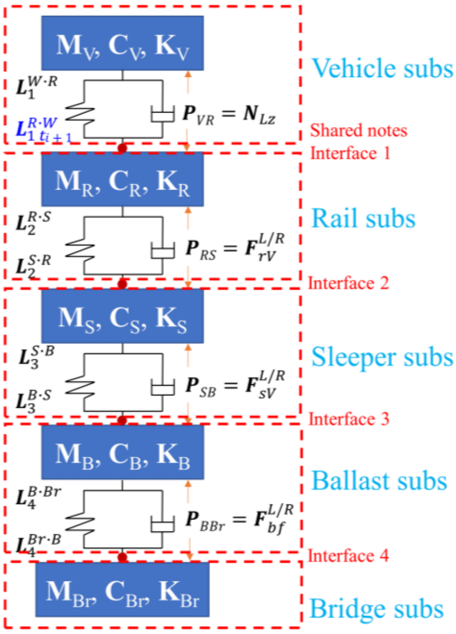

Fig. 4 Schematic diagram of the partitioned computation for VRBS.

3 The proposed non-iterative partitioned method

The non-iterative partitioned computational method for a time-variant dynamic system is proposed in this section. Specifically, the governing equations of the five subsystems are first condensed by using the Newmark scheme to simplify the subsystem-solving expressions (i.e., multi-partitioned structural analyzers in Section 3.1). Subsequently, the velocity increment of each time step can be computed based on the initial subsystem information in Section 3.2. Then, four-link forces are calculated via the velocity continuity conditions (i.e., the interface solver in Section 3.3). Finally, the proposed method is used to obtain all responses of the system.

3.1 *Multiple partitioned structural analyzers*

The Newmark method with strict energy stability demonstration [37] is employed to solve the governing equations of the five independent subsystems. Considering the equation similarity (As shown in Eqs. (1) ~ (5)), the rail-subsystem governing equation (i.e., Eq. (2)) is chosen as an illustrative example to demonstrate the derivation process of dynamic equations in a compact form. Incremental expressions of the displacement and velocity for the Newmark method are:

$$\Delta \boldsymbol{U}_{t_{i+1}} = \frac{\beta \Delta h}{\gamma} \Delta \dot{\boldsymbol{U}}_{t_{i+1}} + \Delta h \dot{\boldsymbol{U}}_{t_i} + \frac{\gamma - 2\beta}{2\gamma} \Delta h^2 \ddot{\boldsymbol{U}}_{t_i} \tag{10}$$

$$\Delta \ddot{\boldsymbol{U}}_{t_{i+1}} = \frac{1}{\gamma \Delta h} \Delta \dot{\boldsymbol{U}}_{t_{i+1}} - \frac{1}{\gamma} \ddot{\boldsymbol{U}}_{t_i} \tag{11}$$

where the algorithmic parameters γ and β are employed to control the accuracy, stability, and integration scheme type (explicit or implicit) of the Newmark method. Substituting Eqs. (10) and (11) into the governing equation of the rail subsystem without damping (i.e., Eq. (2)), the incremental form of the equation can be derived as follows:

$$\boldsymbol{K}_R^* \Delta \dot{\boldsymbol{U}}_{(R,t_{i+1})} + \Delta \boldsymbol{R}_{(RVS,t_{i+1})} = \Delta \boldsymbol{F}_{(R,t_{i+1})} \tag{12a}$$

$$\boldsymbol{K}_R^* = \frac{1}{\gamma \Delta h} \boldsymbol{M}_R + \frac{\beta \Delta h}{\gamma} \boldsymbol{K}_R , \tag{12b}$$

$$\Delta \boldsymbol{R}_{(RVS,t_{i+1})} = \left(\boldsymbol{L}_{1t_{i+1}}^{R\bullet W} \right)^T \Delta \boldsymbol{P}_{(VR,t_{i+1})} + \left(\boldsymbol{L}_2^{R\bullet S} \right)^T \Delta \boldsymbol{P}_{(RS,t_{i+1})} \tag{12c}$$

$$\Delta\boldsymbol{F}_{(R,t_{i+1})}=\Delta\boldsymbol{P}_{(RE,t_{i+1})}-\boldsymbol{K}_R\left(\frac{\gamma-2\beta}{2\gamma}\Delta h^2\ddot{\boldsymbol{U}}_{(R,t_i)}+\Delta h\dot{\boldsymbol{U}}_{(R,t_i)}\right)+\frac{1}{\gamma}\boldsymbol{M}_R\ddot{\boldsymbol{U}}_{(R,t_i)} \quad (12d)$$

where $\Delta\boldsymbol{R}_{(RVS,\,t_{i+1})}$ refers to the time-varying link force applied to the rail subsystem, originating from the vehicle subsystem and the sleeper subsystem. To simplify the presentation, Eqs. (11) - (12) are rewritten in a compact form as follows:

$$\begin{gathered}\mathbb{K}_R^*\Delta\mathbb{U}_{(R,t_{i+1})}+\Delta\boldsymbol{R}_{(R,t_{i+1})}=\mathbb{F}_{(RE,t_{i+1})}\\ \mathbb{F}_{(RE,t_{i+1})}=\Delta\mathbb{P}_{(RE,t_{i+1})}-\mathbb{N}_R\mathbb{U}_{(R,t_i)}\end{gathered} \quad (13a)$$

$$\mathbb{K}_R^*=\begin{bmatrix}\boldsymbol{I} & -\frac{\beta\Delta h}{\gamma}\boldsymbol{I} & \boldsymbol{0}\\ \boldsymbol{0} & \boldsymbol{K}_R^* & \boldsymbol{0}\\ \boldsymbol{0} & -\frac{1}{\gamma\Delta h}\boldsymbol{I} & \boldsymbol{I}\end{bmatrix} \quad \Delta\mathbb{U}_{(R,t_{i+1})}=\begin{bmatrix}\Delta\boldsymbol{U}_{(R,t_{i+1})}\\ \Delta\dot{\boldsymbol{U}}_{(R,t_{i+1})}\\ \Delta\ddot{\boldsymbol{U}}_{(R,t_{i+1})}\end{bmatrix} \quad (13b, c)$$

$$\Delta\boldsymbol{R}_{(R,t_{i+1})}=\begin{bmatrix}\boldsymbol{0}\\ \Delta\boldsymbol{R}_{(RVS,t_{i+1})}\\ \boldsymbol{0}\end{bmatrix} \qquad \Delta\mathbb{P}_{(RE,t_{i+1})}=\begin{bmatrix}\boldsymbol{0}\\ \Delta\boldsymbol{P}_{(RE,t_{i+1})}+\Delta\boldsymbol{Fr}\\ \boldsymbol{0}\end{bmatrix} \quad (13d, e)$$

$$\mathbb{N}_R=\begin{bmatrix}\boldsymbol{0} & -\Delta h\boldsymbol{I} & -\frac{\gamma-2\beta}{2\gamma}\Delta h^2\boldsymbol{I}\\ \boldsymbol{0} & \Delta h\boldsymbol{K}_R & \frac{\gamma-2\beta}{2\gamma}\Delta h^2\boldsymbol{K}_R-\frac{1}{\gamma}\boldsymbol{M}_R\\ \boldsymbol{0} & \boldsymbol{0} & \frac{1}{\gamma}\boldsymbol{I}\end{bmatrix} \qquad \mathbb{U}_{(R,t_i)}=\begin{bmatrix}\boldsymbol{U}_{(R,t_i)}\\ \dot{\boldsymbol{U}}_{(R,t_i)}\\ \ddot{\boldsymbol{U}}_{(R,t_i)}\end{bmatrix} \quad (13f, g)$$

where $\boldsymbol{0}$ and $\boldsymbol{I}$ are, respectively, the zero matrix and identity matrix, with the same dimension as the stiffness matrix $\boldsymbol{K}$. By referring to the derivation of the rail incremental form, i.e., Eqs, (12) and (13), the compact forms of all subsystems can be derived as follows:

$$\begin{cases}\mathbb{K}_V^*\Delta\mathbb{U}_{(V,t_{i+1})}+\Delta\boldsymbol{R}_{(V,t_{i+1})}=\mathbb{F}_{(VE,t_{i+1})}\\ \mathbb{K}_R^*\Delta\mathbb{U}_{(R,t_{i+1})}+\Delta\boldsymbol{R}_{(R,t_{i+1})}=\mathbb{F}_{(RE,t_{i+1})}\\ \mathbb{K}_S^*\Delta\mathbb{U}_{(S,t_{i+1})}+\Delta\boldsymbol{R}_{(S,t_{i+1})}=\mathbb{F}_{(SE,t_{i+1})}\\ \mathbb{K}_B^*\Delta\mathbb{U}_{(B,t_{i+1})}+\Delta\boldsymbol{R}_{(B,t_{i+1})}=\mathbb{F}_{(BE,t_{i+1})}\\ \mathbb{K}_{Br}^*\Delta\mathbb{U}_{(Br,t_{i+1})}+\Delta\boldsymbol{R}_{(Br,t_{i+1})}=\mathbb{F}_{(BrE,t_{i+1})}\end{cases} \quad (14)$$

where $\Delta\boldsymbol{R}$ is the link force vectors applied to the corresponding subsystem and they can be derived in a similar manner as follows:

$$\Delta\boldsymbol{R}_{(VR,t_{i+1})}=\left(\boldsymbol{L}_1^{W\bullet R}\right)^T\Delta\boldsymbol{P}_{(VR,t_{i+1})} \tag{15a}$$

$$\Delta\boldsymbol{R}_{(RVS,t_{i+1})}=\left(\boldsymbol{L}_{1t_{i+1}}^{R\bullet W}\right)^T\Delta\boldsymbol{P}_{(VR,t_{i+1})}+\left(\boldsymbol{L}_2^{R\bullet S}\right)^T\Delta\boldsymbol{P}_{(RS,t_{i+1})} \tag{15b}$$

$$\Delta\boldsymbol{R}_{(SRB,t_{i+1})}=\left(\boldsymbol{L}_2^{S\bullet R}\right)^T\Delta\boldsymbol{P}_{(RS,t_{i+1})}+\left(\boldsymbol{L}_3^{S\bullet B}\right)^T\Delta\boldsymbol{P}_{(SB,t_{i+1})} \tag{15c}$$

$$\Delta\boldsymbol{R}_{(BSBr,t_{i+1})}=\left(\boldsymbol{L}_3^{B\bullet S}\right)^T\Delta\boldsymbol{P}_{(SB,t_{i+1})}+\left(\boldsymbol{L}_4^{B\bullet Br}\right)^T\Delta\boldsymbol{P}_{(BBr,t_{i+1})} \tag{15d}$$

$$\Delta\boldsymbol{R}_{(BrB,t_{i+1})}=\left(\boldsymbol{L}_4^{Br\bullet B}\right)^T\Delta\boldsymbol{P}_{(BBr,t_{i+1})} \tag{15e}$$

where $\Delta\boldsymbol{R}_{(VR,\,t_{i+1})}$, $\Delta\boldsymbol{R}_{(SRB,\,t_{i+1})}$, $\Delta\boldsymbol{R}_{(BSBr,\,t_{i+1})}$, and $\Delta\boldsymbol{R}_{(BrB,\,t_{i+1})}$ denote the force vectors applied to the vehicle, sleeper, ballast, and bridge subsystems, respectively. $\Delta\boldsymbol{P}_{(VR,\,t_{i+1})}$, $\Delta\boldsymbol{P}_{(RS,\,t_{i+1})}$, $\Delta\boldsymbol{P}_{(SB,\,t_{i+1})}$, and $\Delta\boldsymbol{P}_{(BrB,\,t_{i+1})}$ are the four-link force vectors to be solved, as shown in Fig. 4. Up to this point, the coupling dynamic system with four unknown link forces (i.e., the multi-partitioned structural analyzers) is built in Eq. (14). Based on the velocity continuity conditions and the velocity increments in a time step obtained in the next section, an interface solver is developed to compute the link forces.

3.2 *Velocity increments within a time step*

Given the similarity of the governing equations, the rail subsystem is employed to illustrate the calculation of velocity increments within a time step Δh. The incremental form for the governing equation of the rail subsystem without damping is rewritten as:

$$\boldsymbol{M}_R\Delta\ddot{\boldsymbol{U}}_{(R,t_{i+1})}+\boldsymbol{K}_R\Delta\boldsymbol{U}_{(R,t_{i+1})}+\Delta\boldsymbol{R}_{(RVS,t_{i+1})}=\Delta\boldsymbol{P}_{(RE,t_{i+1})}+\Delta\boldsymbol{Fr} \tag{16}$$

Substituting incremental forms of the Newmark scheme (i.e., Eqs. (10) and (11)) into Eq. (16), the velocity increment is obtained as follows:

$$\Delta\dot{\boldsymbol{U}}_{(R,t_{i+1})}=\boldsymbol{K}_R^{*^{-1}}\left(\Delta\boldsymbol{P}_{(RE,t_{i+1})}+\Delta\boldsymbol{Fr}-\Delta\boldsymbol{R}_{(RVS,t_{i+1})}-\left(\frac{\gamma-2\beta}{2\gamma}\Delta h^2\boldsymbol{K}_R-\frac{1}{\gamma}\boldsymbol{M}_R\right)\ddot{\boldsymbol{U}}_{(R,t_i)}-\Delta h\boldsymbol{K}_R\dot{\boldsymbol{U}}_{(R,t_i)}\right) \tag{17}$$

Eq. (17) demonstrates that the velocity increment of the rail subsystem can be computed by using the initial information at t_i (e.g., $\dot{\boldsymbol{U}}_{(R,\,t_i)}$ and $\ddot{\boldsymbol{U}}_{(R,\,t_i)}$). To compute the link force, the velocity increment $\Delta\dot{\mathbf{U}}_{t_{i+1}}$ is divided into two parts (i.e., $\Delta\dot{\boldsymbol{U}}_{(R,t_{i+1})}^{Lin}$ and

$\Delta\dot{\boldsymbol{U}}^{Ext}_{(RE,t_{i+1})}$) according to the loading types (i.e., the link force $\Delta\boldsymbol{R}_{(RVS,t_{i+1})}$ and the external force $\Delta\boldsymbol{P}_{(RE,t_{i+1})}$) as follows:

$$\Delta\dot{\boldsymbol{U}}_{(R,t_{i+1})} = \Delta\dot{\boldsymbol{U}}^{Lin}_{(R,t_{i+1})} + \Delta\dot{\boldsymbol{U}}^{Ext}_{(RE,t_{i+1})} \tag{18a}$$

$$\Delta\dot{\boldsymbol{U}}^{Lin}_{(R,t_{i+1})} = -\boldsymbol{K}_R^{*\,-1}\Delta\boldsymbol{R}_{(RVS,t_{i+1})} \tag{18b}$$

$$\Delta\dot{\boldsymbol{U}}^{Ext}_{(RE,t_{i+1})} = \boldsymbol{K}_R^{*\,-1}\left(\Delta\boldsymbol{P}_{(RE,t_{i+1})} + \Delta\boldsymbol{Fr} - \boldsymbol{R}_R^{*}\ddot{\boldsymbol{U}}_{(R,t_i)} - \Delta h\boldsymbol{K}_R\dot{\boldsymbol{U}}_{(R,t_i)}\right) \tag{18c}$$

For linear systems, all coefficients in Eq. (17) are constants that can be pre-determined before computation. Similarly, the velocity increments for all subsystems can be obtained. The link forces at interfaces are computed in the next section via the obtained velocity increments and the velocity continuity conditions.

3.3 *The interface solver*

The first interface, connecting the vehicle subsystem and the rail subsystem (See Fig. 4), is employed to illustrate the calculation process of the four interface link forces by using the assumed velocity continuity conditions (i.e., Eq. (6)) and the solved velocity increments (i.e., Eq. (18)). The velocity continuity condition at the first interface is rewritten as follows:

$$\boldsymbol{L}_1^{W\bullet R}\left(\Delta\dot{\boldsymbol{U}}^{Lin}_{(V,t_{i+1})} + \Delta\dot{\boldsymbol{U}}^{Ext}_{(VE,t_{i+1})}\right) + \boldsymbol{L}_{1t_{i+1}}^{R\bullet W}\left(\Delta\dot{\boldsymbol{U}}^{Lin}_{(R,t_{i+1})} + \Delta\dot{\boldsymbol{U}}^{Ext}_{(RE,t_{i+1})}\right) = 0 \tag{19}$$

By referring to the results in Eqs. (17) and (18), the vehicle system velocity increments caused by the link forces and external forces are derived as follows:

$$\Delta\dot{\boldsymbol{U}}^{Lin}_{(V,t_{i+1})} = -\boldsymbol{K}_V^{*-1}\left[\left(\boldsymbol{L}_1^{W\bullet R}\right)^T\Delta\boldsymbol{P}_{(VR,t_{i+1})}\right] \tag{20}$$

$$\Delta\dot{\boldsymbol{U}}^{Ext}_{(VE,t_{i+1})} = \boldsymbol{K}_V^{*\,-1}\left(\Delta\boldsymbol{P}_{(VE,t_{i+1})} + \Delta\boldsymbol{Fv} - \boldsymbol{R}_V^{*}\ddot{\boldsymbol{U}}_{(V,t_i)} - \Delta h\boldsymbol{K}_V\dot{\boldsymbol{U}}_{(V,t_i)}\right) \tag{21}$$

where $\boldsymbol{K}_V^{*}$ is the vehicle equivalent stiffness matrix, which has the same form as Eq. (12b). Substituting Eqs. 18(b), 18(c), (21), and (22) into the velocity continuity condition (i.e., Eq. (20)), one has:

$$\Delta\dot{\boldsymbol{U}}^{Ext}_{VR} = \boldsymbol{H}_{V\bullet R}\Delta\boldsymbol{P}_{(VR,t_{i+1})} + \boldsymbol{G}_{W\bullet S}\Delta\boldsymbol{P}_{(RS,t_{i+1})} \tag{22}$$

$$\Delta\dot{\boldsymbol{U}}^{Ext}_{VR} = \boldsymbol{L}_1^{W\bullet R}\Delta\dot{\boldsymbol{U}}^{Ext}_{(VE,t_{i+1})} + \boldsymbol{L}_{1t_{i+1}}^{R\bullet W}\Delta\dot{\boldsymbol{U}}^{Ext}_{(RE,t_{i+1})} \tag{23a}$$

$$\boldsymbol{G}_{W\bullet S}=\boldsymbol{L}_{1t_{i+1}}^{R\bullet W}\boldsymbol{K}_{R}^{*-1}\left(\boldsymbol{L}_{2}^{R\bullet S}\right)^{T} \tag{23b}$$

$$\boldsymbol{H}_{V\bullet R}=\left(\boldsymbol{L}_{1}^{W\bullet R}\boldsymbol{K}_{V}^{*-1}\left(\boldsymbol{L}_{1}^{W\bullet R}\right)^{T}+\boldsymbol{L}_{1t_{i+1}}^{R\bullet W}\boldsymbol{K}_{R}^{*-1}\left(\boldsymbol{L}_{1t_{i+1}}^{R\bullet W}\right)^{T}\right) \tag{23c}$$

All coefficients in Eq. (22) are constant for a linear system, and the velocity increments of the vehicle and rail subsystems caused by the external forces (i.e., Eq. (23 a)) are readily obtained. Similarly, the remaining three interface continuity conditions can also be expressed in the form of link forces.

For the second interface, connecting the railway and sleeper subsystems, one has:

$$\Delta\dot{\boldsymbol{U}}_{RS}^{Ext}=\boldsymbol{H}_{R\bullet S}\Delta\boldsymbol{P}_{RS}+\boldsymbol{G}_{S\bullet W}\Delta\boldsymbol{P}_{(VR,t_{i+1})}+\boldsymbol{G}_{R\bullet B}\Delta\boldsymbol{P}_{SB} \tag{24}$$

$$\Delta\dot{\boldsymbol{U}}_{RS}^{Ext}=\boldsymbol{L}_{2}^{R\bullet S}\Delta\dot{\boldsymbol{U}}_{(RE,t_{i+1})}^{Ext}+\boldsymbol{L}_{2}^{S\bullet R}\Delta\dot{\boldsymbol{U}}_{(SE,t_{i+1})}^{Ext} \tag{25a}$$

$$\boldsymbol{G}_{S\bullet W}=\boldsymbol{L}_{2}^{R\bullet S}\boldsymbol{K}_{R}^{*-1}\left(\boldsymbol{L}_{1t_{i+1}}^{R\bullet W}\right)^{T} \tag{25b}$$

$$\boldsymbol{G}_{R\bullet B}=\boldsymbol{L}_{2}^{S\bullet R}\boldsymbol{K}_{S}^{*-1}\left(\boldsymbol{L}_{3}^{S\bullet B}\right)^{T} \tag{25c}$$

$$\boldsymbol{H}_{R\bullet S}=\left(\boldsymbol{L}_{2}^{R\bullet S}\boldsymbol{K}_{R}^{*-1}\left(\boldsymbol{L}_{2}^{R\bullet S}\right)^{T}+\boldsymbol{L}_{2}^{S\bullet R}\boldsymbol{K}_{S}^{*-1}\left(\boldsymbol{L}_{2}^{S\bullet R}\right)^{T}\right) \tag{25d}$$

For the third interface, connecting the sleeper and ballast subsystems, one has:

$$\Delta\dot{\boldsymbol{U}}_{SB}^{Ext}=\boldsymbol{H}_{S\bullet B}\Delta\boldsymbol{P}_{SB}+\boldsymbol{G}_{B\bullet R}\Delta\boldsymbol{P}_{RS}+\boldsymbol{G}_{S\bullet Br}\Delta\boldsymbol{P}_{BBr} \tag{26}$$

$$\Delta\dot{\boldsymbol{U}}_{SB}^{Ext}=\boldsymbol{L}_{3}^{S\bullet B}\Delta\dot{\boldsymbol{U}}_{(SE,t_{i+1})}^{Ext}+\boldsymbol{L}_{3}^{B\bullet S}\Delta\dot{\boldsymbol{U}}_{(BE,t_{i+1})}^{Ext} \tag{27a}$$

$$\boldsymbol{G}_{B\bullet R}=\boldsymbol{L}_{3}^{S\bullet B}\boldsymbol{K}_{S}^{*-1}\left(\boldsymbol{L}_{2}^{S\bullet R}\right)^{T} \tag{27b}$$

$$\boldsymbol{G}_{S\bullet Br}=\boldsymbol{L}_{3}^{B\bullet S}\boldsymbol{K}_{B}^{*-1}\left(\boldsymbol{L}_{4}^{B\bullet Br}\right)^{T} \tag{27c}$$

$$\boldsymbol{H}_{S\bullet B}=\left(\boldsymbol{L}_{3}^{S\bullet B}\boldsymbol{K}_{S}^{*-1}\left(\boldsymbol{L}_{3}^{S\bullet B}\right)^{T}+\boldsymbol{L}_{3}^{B\bullet S}\boldsymbol{K}_{B}^{*-1}\left(\boldsymbol{L}_{3}^{B\bullet S}\right)^{T}\right) \tag{27d}$$

For the fourth interface, connecting the ballast and bridge subsystems, one has:

$$\Delta\dot{\boldsymbol{U}}_{BBr}^{Ext}=\boldsymbol{H}_{B\bullet Br}\Delta\boldsymbol{P}_{BBr}+\boldsymbol{G}_{Br\bullet S}\Delta\boldsymbol{P}_{SB} \tag{28}$$

$$\Delta\dot{\boldsymbol{U}}_{BBr}^{Ext}=\boldsymbol{L}_{4}^{B\bullet Br}\Delta\dot{\boldsymbol{U}}_{(BE,t_{i+1})}^{Ext}+\boldsymbol{L}_{4}^{Br\bullet B}\Delta\dot{\boldsymbol{U}}_{(BrE,t_{i+1})}^{Ext} \tag{29a}$$

$$\boldsymbol{G}_{Br\bullet S}=\boldsymbol{L}_{4}^{B\bullet Br}\boldsymbol{K}_{B}^{*-1}\left(\boldsymbol{L}_{3}^{B\bullet S}\right)^{T} \tag{29b}$$

$$\boldsymbol{H}_{B\bullet Br}=\left(\boldsymbol{L}_{4}^{B\bullet Br}\boldsymbol{K}_{B}^{*-1}\left(\boldsymbol{L}_{4}^{B\bullet Br}\right)^{T}+\boldsymbol{L}_{4}^{Br\bullet B}\boldsymbol{K}_{Br}^{*-1}\left(\boldsymbol{L}_{4}^{Br\bullet B}\right)^{T}\right) \tag{29c}$$

Since all quantities in Eqs. (22) to (29) can be determined via given information, the four-link force vectors (i.e., $\Delta\boldsymbol{P}_{(VR,t_{i+1})}$, $\Delta\boldsymbol{P}_{(RS,t_{i+1})}$, $\Delta\boldsymbol{P}_{(SB,t_{i+1})}$, and $\Delta\boldsymbol{P}_{(BBr,t_{i+1})}$, in Fig. 4) can be directly obtained by solving the four linear equations (i.e., the interface solver consists of Eqs. (22), (24), (26), and (28)). Once the link forces are determined, the coupling system (i.e., Eq. (14)) is decomposed into five independent subsystems (see Fig. 4), and the responses of all subsystems at t_{i+1} can be solved independently via Eq. (14). The computational procedure of the proposed method is given in Appendix B.

It is worth noting that the above five subsystem matrices, involved in the derivation process, can be substituted with alternative dynamic systems [15]. Moreover, arbitrary subsystems can serve as time-variant subsystems and updated time-related loadings (e.g., $\Delta\mathbf{F}\boldsymbol{r}$ and $\Delta\mathbf{F}\boldsymbol{v}$) can be derived from the interconnected subsystems with relative motion. By employing the developed interface solver in the proposed method, a time-variant dynamic system can be decoupled into independent subsystems, and all responses of all subsystems can be solved by the developed multi-partitioned structural analyzers. Therefore, the proposed method is applicable to other time-variant dynamic systems as well.

In addition, VRBS can be separated into more subsystems by increasing more interfaces at corresponding positions, and updated multivariate linear equations can be used to solve the unknown link forces. Conversely, merging interconnected subsystems can decrease the number of subsystems and interfaces. For instance, by merging the ballast and bridge subsystems, the resulting partitioned system will consist of only four subsystems, three interfaces, and three-link force vectors. For two subsystems, only one interface and one link force vector exist in the portioned system. The derivation process of the two-subsystem system is given in Appendix C, demonstrating the simplicity of the computational procedure. It is worth noting that the built VRBS includes essentially five independent mathematical matrices that represent different physical subsystems, and they can also represent other more complex physical systems when corresponding physical properties are assigned to the matrices. On the contrary, in Appendix C, a two-subsystem model consisting of the spring-mass subsystem and the continuous beam subsystem (as shown in Fig. A3) is built to demonstrate the applicability of solving other time-variant dynamic systems.

In the interface solver, solving linear equations is essential to computing link forces, leading to increased computational time proportional to the number of subsystems, as elaborated in Section 5.3. Additionally, while energy dissipation doesn't occur at interfaces, exceedingly minute link force values emerge in results due to floating-point operation errors, as discussed in Section 5.1. These drawbacks restrict us from incorporating an excessive number of subsystems into the calculation.

4 Proof of computational stability based on the system energy

The energy conservation property, including the interface pseudo-energy and the interface mechanical energy, is investigated in this section to prove the computational stability of the proposed method.

4.1 The interface pseudo-energy

The following pseudo-energy norm of a dynamic system without external excitations (solved by the Newmark method [37]) is widely used to investigate the computational stability of partitioned systems. Further details on the pseudo-energy can be found in [33,38].

$$\frac{1}{2}\left[\ddot{\boldsymbol{U}}_k^T \bar{\boldsymbol{A}}_k \ddot{\boldsymbol{U}}_k + \dot{\boldsymbol{U}}_k^T \boldsymbol{K}_k \dot{\boldsymbol{U}}_k\right]_{t_i}^{t_{i+1}} = -\left(\gamma - \frac{1}{2}\right)\Delta\ddot{\boldsymbol{U}}^T_{(k,t_{i+1})}\bar{\boldsymbol{A}}_k\Delta\ddot{\boldsymbol{U}}_{(k,t_{i+1})} + \frac{1}{\Delta h}\Delta\dot{\boldsymbol{U}}^T_{(k,t_{i+1})}\Delta\mathbb{R}_{(k,t_{i+1})} \tag{30a}$$

$$\bar{\boldsymbol{A}}_k = \boldsymbol{M}_k + \Delta h_k^2\left(\beta - \frac{1}{2}\gamma\right)\boldsymbol{K}_k, \qquad \Delta\mathbb{R}_{(k,t_{i+1})} = \Delta\boldsymbol{P}_{(kE,t_{i+1})} + \Delta\boldsymbol{R}_{(k,t_{i+1})} \tag{30 b, c}$$

where k is the subsystem number; the symbol $[\,]_{t_i}^{t_{i+1}}$ is the increment of kinematic quantities from t_i to t_{i+1}; and $\Delta\mathbb{R}_{(k,t_{i+1})}$ includes the link forces $\Delta\boldsymbol{R}_{(k,t_{i+1})}$ and external excitation $\Delta\boldsymbol{P}_{(kE,t_{i+1})}$, as shown in Eqs. (1) ~ (5). The pseudo-energy incremental is:

$$\Delta E_{kin}^k + \Delta E_{\mathrm{int}}^k = \Delta E_{diss}^k + \Delta E_{ext}^k \tag{31a}$$

$$\Delta E_{kin}^k = \frac{1}{2}\left[\ddot{\boldsymbol{U}}_k^T \bar{\boldsymbol{A}}_k \ddot{\boldsymbol{U}}_k\right]_{t_i}^{t_{i+1}}, \quad \Delta E_{int}^k = \frac{1}{2}\left[\dot{\boldsymbol{U}}_k^T \boldsymbol{K}_k \dot{\boldsymbol{U}}_k\right]_{t_i}^{t_{i+1}} \tag{31b, c}$$

$$\Delta E_{diss}^{k}=-\left(\gamma-\frac{1}{2}\right)\Delta\ddot{\boldsymbol{U}}_{(k,t_{i+1})}^{T}\bar{\boldsymbol{A}}_{k}\Delta\ddot{\boldsymbol{U}}_{(k,t_{i+1})},\quad \Delta E_{ext}^{k}=\frac{1}{\Delta h}\Delta\dot{\boldsymbol{U}}_{(k,t_{i+1})}^{T}\Delta\mathbb{R}_{t_{n+1}}^{k} \tag{31d, e}$$

where ΔE_{kin}^{k}, ΔE_{int}^{k}, ΔE_{diss}^{k}, and ΔE_{ext}^{k} refer to the pseudo kinetic energy, the pseudo-potential energy, the pseudo dissipation energy, and the pseudo loading energy of the k^{th} subsystem at Δh, respectively. According to the link forces in Eq. (15) or Fig. 4, the pseudo-loading energy generated by link forces (i.e., ΔE_{ext}^{k}) is:

$$\Delta E_{link}^{k}=\Delta E_{ext}^{k}=\frac{1}{\Delta h}\Delta\dot{\boldsymbol{U}}_{(k,t_{i+1})}^{T}\Delta\boldsymbol{R}_{(k,t_{i+1})} \tag{32}$$

According to the stability conditions in [38] (i.e., $\gamma\geqslant 1/2$ and $\bar{\boldsymbol{A}}$ is positive definite), individual subsystem responses under forces are stable if $\Delta E_{ext}^{k}\leqslant 0$. Referring to Eq. (31), the total pseudo-energy for VRBS with five subsystems is:

$$\sum_{k=1}^{5}\left(\Delta E_{kin}^{k}+\Delta E_{int}^{k}\right)=\sum_{k=1}^{5}\left(\Delta E_{diss}^{k}\right)+\Delta E_{link} \tag{33}$$

The total pseudo-loading energy dissipated at all interfaces is:

$$\Delta E_{link}=\sum_{l=1}^{4}\left(\Delta E_{ext}^{k\bullet j}+\Delta E_{ext}^{j\bullet k}\right) \tag{34}$$

where the superscripts stand for two interconnected subsystem numbers. For instance, for the first interface, k and j denote the vehicle (V) and rail (R) subsystems, respectively. Substituting Eq. (32) into Eq. (34), the total pseudo-loading energy caused by four-link forces (i.e., Eq. (15)) is derived as follows:

$$\begin{aligned}
\Delta E_{link}=&\frac{1}{\Delta h}\Delta\dot{\boldsymbol{U}}_{(V,t_{i+1})}^{T}\left(\boldsymbol{L}_{1}^{W\bullet R}\right)^{T}\Delta\boldsymbol{P}_{(VR,t_{i+1})}+\\
&\frac{1}{\Delta h}\Delta\dot{\boldsymbol{U}}_{(R,t_{i+1})}^{T}\left(\left(\boldsymbol{L}_{1t_{i+1}}^{R\bullet W}\right)^{T}\Delta\boldsymbol{P}_{(VR,t_{i+1})}+\left(\boldsymbol{L}_{2}^{R\bullet S}\right)^{T}\Delta\boldsymbol{P}_{(RS,t_{i+1})}\right)+\\
&\frac{1}{\Delta h}\Delta\dot{\boldsymbol{U}}_{(S,t_{i+1})}^{T}\left(\left(\boldsymbol{L}_{2}^{S\bullet R}\right)^{T}\Delta\boldsymbol{P}_{(RS,t_{i+1})}+\left(\boldsymbol{L}_{3}^{S\bullet B}\right)^{T}\Delta\boldsymbol{P}_{(SB,t_{i+1})}\right)+\\
&\frac{1}{\Delta h}\Delta\dot{\boldsymbol{U}}_{(B,t_{i+1})}^{T}\left(\left(\boldsymbol{L}_{3}^{B\bullet S}\right)^{T}\Delta\boldsymbol{P}_{(SB,t_{i+1})}+\left(\boldsymbol{L}_{4}^{B\bullet Br}\right)^{T}\Delta\boldsymbol{P}_{(BBr,t_{i+1})}\right)+\\
&\frac{1}{\Delta h}\Delta\dot{\boldsymbol{U}}_{(Br,t_{i+1})}^{T}\left(\left(\boldsymbol{L}_{4}^{Br\bullet B}\right)^{T}\Delta\boldsymbol{P}_{(BBr,t_{i+1})}\right)
\end{aligned} \tag{35}$$

The total pseudo-loading energy is simplified as follows:

$$\Delta E_{link} = \frac{1}{\Delta h}\begin{bmatrix} \left(\Delta\dot{\boldsymbol{U}}_{(V,t_{i+1})}^{T}\left(\boldsymbol{L}_{1}^{W\bullet R}\right)^{T} + \Delta\dot{\boldsymbol{U}}_{(R,t_{i+1})}^{T}\left(\boldsymbol{L}_{1t_{i+1}}^{R\bullet W}\right)^{T}\right)\Delta\boldsymbol{P}_{(VR,t_{i+1})} + \\ \left(\Delta\dot{\boldsymbol{U}}_{(R,t_{i+1})}^{T}\left(\boldsymbol{L}_{2}^{R\bullet S}\right)^{T} + \Delta\dot{\boldsymbol{U}}_{(S,t_{i+1})}^{T}\left(\boldsymbol{L}_{2}^{S\bullet R}\right)^{T}\right)\Delta\boldsymbol{P}_{(RS,t_{i+1})} + \\ \left(\Delta\dot{\boldsymbol{U}}_{(S,t_{i+1})}^{T}\left(\boldsymbol{L}_{3}^{S\bullet B}\right)^{T} + \Delta\dot{\boldsymbol{U}}_{(B,t_{i+1})}^{T}\left(\boldsymbol{L}_{3}^{B\bullet S}\right)^{T}\right)\Delta\boldsymbol{P}_{(SB,t_{i+1})} + \\ \left(\Delta\dot{\boldsymbol{U}}_{(B,t_{i+1})}^{T}\left(\boldsymbol{L}_{4}^{B\bullet Br}\right)^{T} + \Delta\dot{\boldsymbol{U}}_{(Br,t_{i+1})}^{T}\left(\boldsymbol{L}_{4}^{Br\bullet B}\right)^{T}\right)\Delta\boldsymbol{P}_{(BBr,t_{i+1})} \end{bmatrix} \tag{36}$$

Substituting the velocity continuity conditions (i.e., Eqs. (6) ~ (9)) into Eq. (33), the total pseudo loading energy within the duration from t_0 to t_n is:

$$\Delta E_{LINK} = \int_{t_0}^{t_n} \Delta E_{link} = 0 \tag{37}$$

Therefore, if the assumed velocity continuity conditions and the Newmark scheme are ensured in the computation process, the total pseudo-loading energy will be equal to zero and will not be affected by the algorithmic parameters (γ and β). Consequently, the stability of the proposed method can be guaranteed in the partitioned computation.

4.2 The interface mechanical energy

The following system mechanical energy in [33,37,39] is also used to investigate the proposed method's stability. Note that external forces and damping forces are not considered in the system.

$$\begin{aligned} \frac{1}{2}\left[\dot{\boldsymbol{U}}^{T}\boldsymbol{M}\dot{\boldsymbol{U}} + \boldsymbol{U}^{T}\boldsymbol{K}\boldsymbol{U}\right]_{t_i}^{t_{i+1}} &= \Delta\boldsymbol{U}^{T}\left(\gamma\boldsymbol{P}_{t_{n+1}} + (1-\gamma)\boldsymbol{P}_{t_n}\right) - \left(\gamma - \frac{1}{2}\right)\Delta\boldsymbol{U}^{T}\boldsymbol{K}\Delta\boldsymbol{U} \\ -\left(\gamma-\frac{1}{2}\right)&\left(\beta - \frac{1}{2}\gamma\right)\Delta h^{2}\Delta\ddot{\boldsymbol{U}}^{T}\boldsymbol{M}\Delta\ddot{\boldsymbol{U}} - \left(\beta-\frac{1}{2}\gamma\right)\frac{1}{2}\Delta h^{2}\left[\ddot{\boldsymbol{U}}^{T}\boldsymbol{M}\ddot{\boldsymbol{U}}\right]_{t_i}^{t_{i+1}} \end{aligned} \tag{38}$$

The mechanical energy increment of the k^{th} subsystem without external forces is rewritten as follows:

$$\begin{aligned} \Delta\tau_{t_{i+1}}^{k} + \Delta\upsilon_{t_{i+1}}^{k} = \Delta\boldsymbol{U}_{t_{i+1}}^{k^{T}}&\left(\gamma^{k}\boldsymbol{R}_{(k,t_{i+1})} + \left(1-\gamma^{k}\right)\boldsymbol{R}_{(k,t_i)}\right) \\ &-\left(\gamma^{k}-\frac{1}{2}\right)\Delta\boldsymbol{U}_{t_{i+1}}^{k^{T}}\boldsymbol{K}_{k}\Delta\boldsymbol{U}_{t_{i+1}}^{k} \\ &-\left(\gamma^{k}-\frac{1}{2}\right)\left(\beta^{k}-\frac{1}{2}\gamma^{k}\right)\Delta h^{k^{2}}\Delta\ddot{\boldsymbol{U}}_{t_{i+1}}^{k^{T}}\boldsymbol{M}_{k}\Delta\ddot{\boldsymbol{U}}_{t_{i+1}}^{k} \\ &-\left(\beta^{k}-\frac{1}{2}\gamma^{k}\right)\Delta o_{t_{i+1}}^{k} \end{aligned} \tag{39a}$$

$$\Delta\tau_{t_{i+1}}^{k} = \frac{1}{2}\left(\dot{\boldsymbol{U}}_{t_{i+1}}^{k^T}\boldsymbol{M}_k\dot{\boldsymbol{U}}_{t_{i+1}}^{k} - \dot{\boldsymbol{U}}_{t_i}^{k^T}\boldsymbol{M}_k\dot{\boldsymbol{U}}_{t_i}^{k}\right) \tag{39b}$$

$$\Delta\upsilon_{t_{i+1}}^{k} = \frac{1}{2}\left(\boldsymbol{U}_{t_{i+1}}^{k^T}\boldsymbol{K}_k\boldsymbol{U}_{t_{i+1}}^{k} - \boldsymbol{U}_{t_i}^{k^T}\boldsymbol{K}_k\boldsymbol{U}_{t_i}^{k}\right) \tag{39c}$$

$$\Delta o_{t_{i+1}}^{k} = \frac{1}{2}\Delta h^{k^2}\left(\ddot{\boldsymbol{U}}_{t_{i+1}}^{k^T}\boldsymbol{M}_k\ddot{\boldsymbol{U}}_{t_{i+1}}^{k} - \ddot{\boldsymbol{U}}_{t_i}^{k^T}\boldsymbol{M}_k\ddot{\boldsymbol{U}}_{t_i}^{k}\right) \tag{39d}$$

where $\Delta\tau_{t_{i+1}}^{k}$, $\Delta\upsilon_{t_{i+1}}^{k}$, and $\Delta o_{t_{i+1}}^{k}$ refer to the kinetic energy, the potential energy, and the dissipative energy of the k^{th} subsystem, respectively. The total mechanical energy increments for the system with five subsystems and four interfaces are derived as:

$$\Delta Work = \sum_{k=1}^{5}\left(\Delta\tau_{t_{i+1}}^{k} + \Delta\upsilon_{t_{i+1}}^{k}\right) = \Delta W_{link} + \Delta W_{diss} \tag{40a}$$

$$\Delta W_{link} = \sum_{k=1}^{5}\Delta\boldsymbol{U}_{t_{i+1}}^{k^T}\left(\gamma^k\boldsymbol{R}_{(k,t_{i+1})} + \left(1-\gamma^k\right)\boldsymbol{R}_{(k,t_i)}\right) \tag{40b}$$

$$\begin{aligned}\Delta W_{diss} = &-\sum_{k=1}^{5}\left(\gamma^k - \frac{1}{2}\right)\Delta\boldsymbol{U}_{t_{i+1}}^{k^T}\boldsymbol{K}_k\Delta\boldsymbol{U}_{t_{i+1}}^{k} \\ &-\sum_{k=1}^{5}\left(\gamma^k - \frac{1}{2}\right)\left(\beta^k - \frac{1}{2}\gamma^k\right)\Delta h^{k^2}\Delta\ddot{\boldsymbol{U}}_{t_{i+1}}^{k^T}\boldsymbol{M}_k\Delta\ddot{\boldsymbol{U}}_{t_{i+1}}^{k} \\ &-\sum_{k=1}^{5}\left(\beta^k - \frac{1}{2}\gamma^k\right)\Delta o_{t_{i+1}}^{k}\end{aligned} \tag{40c}$$

where ΔW_{link} and ΔW_{diss} are the interface mechanical energy caused by link forces and the algorithmic dissipation energy, respectively [39,40]. The second-order accuracy (i.e., $\gamma^k = 1/2$) is usually required in numerical analysis. Substituting $\gamma^k = 1/2$ into Eq. (39), the total increments of the system mechanical energy are expressed as follows:

$$\Delta Work = \Delta W_{link} - \sum_{k=1}^{5}\left(\beta^k - \frac{1}{4}\right)\Delta o_{t_{i+1}}^{k} \tag{41}$$

The mechanical energy increment ΔW_{link} in the four interfaces is:

$$\Delta W_{link} = \frac{1}{2}\begin{bmatrix}\left(\Delta\boldsymbol{U}_{(V,t_{i+1})}^{T}\left(\boldsymbol{L}_1^{W\bullet R}\right)^T + \Delta\boldsymbol{U}_{(R,t_{i+1})}^{T}\left(\boldsymbol{L}_{1t_{i+1}}^{R\bullet W}\right)^T\right)\left(\boldsymbol{P}_{(VR,t_{i+1})} + \boldsymbol{P}_{(VR,t_i)}\right) + \\ \left(\Delta\boldsymbol{U}_{(R,t_{i+1})}^{T}\left(\boldsymbol{L}_2^{R\bullet S}\right)^T + \Delta\boldsymbol{U}_{(S,t_{i+1})}^{T}\left(\boldsymbol{L}_2^{S\bullet R}\right)^T\right)\left(\boldsymbol{P}_{(RS,t_{i+1})} + \boldsymbol{P}_{(RS,t_i)}\right) + \\ \left(\Delta\boldsymbol{U}_{(S,t_{i+1})}^{T}\left(\boldsymbol{L}_3^{S\bullet B}\right)^T + \Delta\boldsymbol{U}_{(B,t_{i+1})}^{T}\left(\boldsymbol{L}_3^{B\bullet S}\right)^T\right)\left(\boldsymbol{P}_{(SB,t_{i+1})} + \boldsymbol{P}_{(SB,t_i)}\right) + \\ \left(\Delta\boldsymbol{U}_{(B,t_{i+1})}^{T}\left(\boldsymbol{L}_4^{B\bullet Br}\right)^T + \Delta\boldsymbol{U}_{(Br,t_{i+1})}^{T}\left(\boldsymbol{L}_4^{Br\bullet B}\right)^T\right)\left(\boldsymbol{P}_{(BBr,t_{i+1})} + \boldsymbol{P}_{(BBr,t_i)}\right)\end{bmatrix} \tag{42}$$

According to the velocity continuity conditions, i.e., Eqs. (6) ~ (9), one has $\Delta W_{link} = 0$, and the mechanical energy increment ΔW_{link} within the duration from t_0 to t_n is:

$$\Delta W_{LINK} = \int_{t_0}^{t_n} \Delta W_{link} = 0 \tag{43}$$

When the parameters (i.e., $\beta^k = 1/4$) are thus employed in all subsystems, the total system mechanical energy is conservative (i.e., $\Delta Work = 0$).

5 Numerical demonstrations of the proposed method

To comprehensively evaluate the proposed method in terms of computational stability, accuracy and efficiency, a detailed investigation of a two-dimensional (2D) VRBS constructed in Section 2.1 is performed. VRBS is separated into five subsystems based on their properties, and the continuity conditions of the four interfaces are assumed between the interconnected subsystems, as shown in Fig. 5. A global model (i.e., an unpartitioned model), a widely used model [27], is also constructed here for comparison, and the large global system matrix necessitates reassembly and recalculation at each time step. The 65-meter rail subsystem and 32-meter bridge subsystem, as depicted in Fig. 5, are simulated via plane beam elements, with 650 and 64 elements, respectively. The numbers of sleepers and ballasts are both 65, with a longitudinal spacing of 0.5 m. The springs at the two-side subgrade are fixed at the bottom. Three different vertical initial velocities of the vehicle (i.e., V = 0, 5, and 10 m/s) are analyzed. The vehicle travels at a constant speed of v_0 = 100 m/s, employing a time-step size of Δh = 0.001 s, and the total calculation time is 0.48 s. The relevant parameter values for the two models (i.e., the global model and partitioned model) are presented in Table 2, which are given in Appendix D. The initial mechanical energy and initial pseudo energy for the two models are, respectively, W_0 = 146954.4 J and E_0 = 2274103.82 J when V = 0 m/s.

Comparative study of the numerical results obtained from the two models is performed in the following sections. More specifically, the total mechanical energy and pseudo-energy of the partitioned system without damping and irregularities are first gathered to discuss the proposed method's stability. Subsequently, for the designated subsystem points at the mid-span section (i.e., $\boldsymbol{R}_1$, $\boldsymbol{R}_2$, $\boldsymbol{R}_3$, $\boldsymbol{R}_4$, and $\boldsymbol{R}_5$, as marked in Fig. 5), acceleration responses of the two models are used to assess the proposed method's accuracy, and different integration schemes in different subsystems are analyzed. Finally, the computational efficiency of the system considering different subsystem numbers and the number of DOFs in different subsystems is compared.

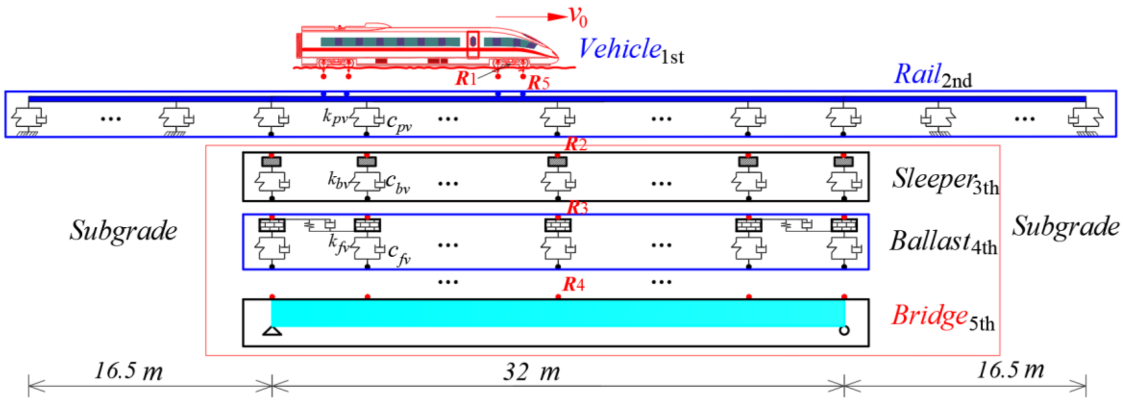

Fig. 5. A partitioned vehicle-rail-sleeper-ballast-bridge vertical system

5.1 Investigation of computational stability

1) *Interface pseudo-energy*

The total interface pseudo-energy caused by link forces (i.e., ΔE_{link} in Eq. (36)), as depicted in Fig. 6, is collected to investigate the computational stability of the proposed method. Two integration schemes are discussed in the stability analysis: Case I, single-implicit Newmark integration schemes with the parameter combination (γ = 1/2 and β = 1/4) are used in all subsystem calculations; Case II, by modifying the vehicle subsystem integration parameter combinations in Case I to be (γ = 1/2 and β = 1/6), the explicit/implicit hybrid calculation schemes are performed in Case II. The theoretical interface pseudo-energy for the two cases should be zero and this can be directly derived from Eq. (37). However, tiny values of ΔE_{link} for the two cases under different vertical initial velocities are observed in Fig. 6. It is worth noting that the calculated pseudo-energy is amplified 1000 times by the time step size Δh, as seen in Eq. (36). When compared with the initial input pseudo-energy E_0 = 2274103.82 J, the amplified ΔE_{link} remains minuscule, as shown in Fig. 6. For the two cases under different initial velocities, suggesting that these discrepancies are attributed to floating-point operation errors. Therefore, the proposed method exhibits the energy conservative property in terms of the interface pseudo-energy.

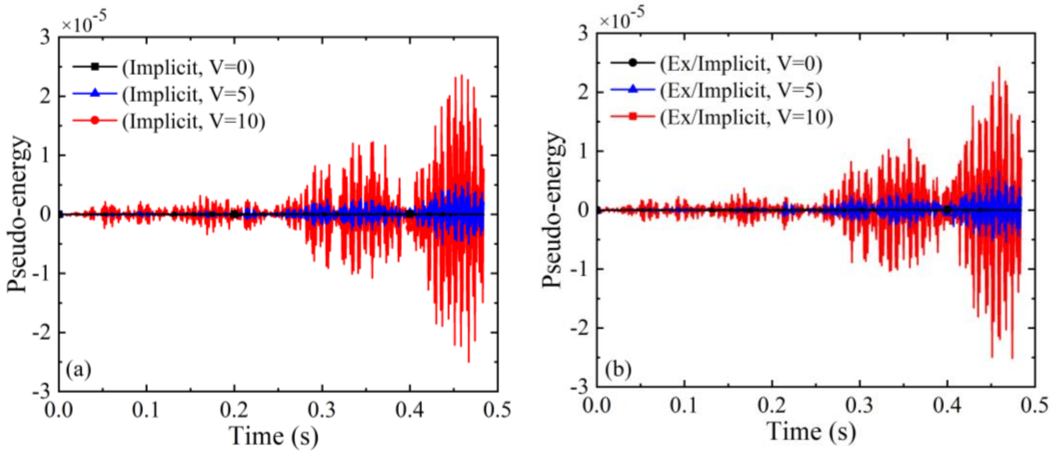

Fig. 6. The interface pseudo energy of the partitioned system: (a) single-implicit Newmark integration schemes with the parameter combination (γ = 1/2 and β = 1/4) and (b) the explicit/implicit hybrid calculation schemes

2) *Interface mechanical energy*

The interface mechanical energy caused by link forces (i.e., ΔW_{link} in Eq. (42)) and the algorithmic dissipation energy of the partitioned system (i.e., ΔW_{diss} in Eq. (40c)), as depicted in Fig. 7, are collected to discuss the proposed method's stability. It is shown that the total ΔW_{link} of the two cases, as shown in Fig. 7(a) and (b), are extremely small and negligible compared with the initial system energy (W_0 = 146954.4 J). The initial vertical vehicle velocity and the used integration schemes affect ΔW_{link}, but the variation in its value is still extremely small. According to the velocity continuity conditions, the theoretical value of ΔW_{link} should be zero, as shown in Eq. (43). However, the tiny ΔW_{link} is presented in the figure due to the floating-point operation errors. Moreover, due to the parameter combination (γ = 1/2 and β = 1/4) in Case I, it is known from Eq. (40c) that ΔW_{diss} is always zero. Therefore, we present only the values of ΔW_{diss} for Case II in Fig. 7. Fig. 7(c) shows that ΔW_{diss}, caused by the parameter β, gradually increases with the increase of initial vehicle vertical velocities, which is often used to filter high-frequency spurious vibrations [8,9]. Therefore, the proposed method possesses the property of mechanical energy conservation, ensuring zero mechanical energy at the interfaces of interconnected subsystems.

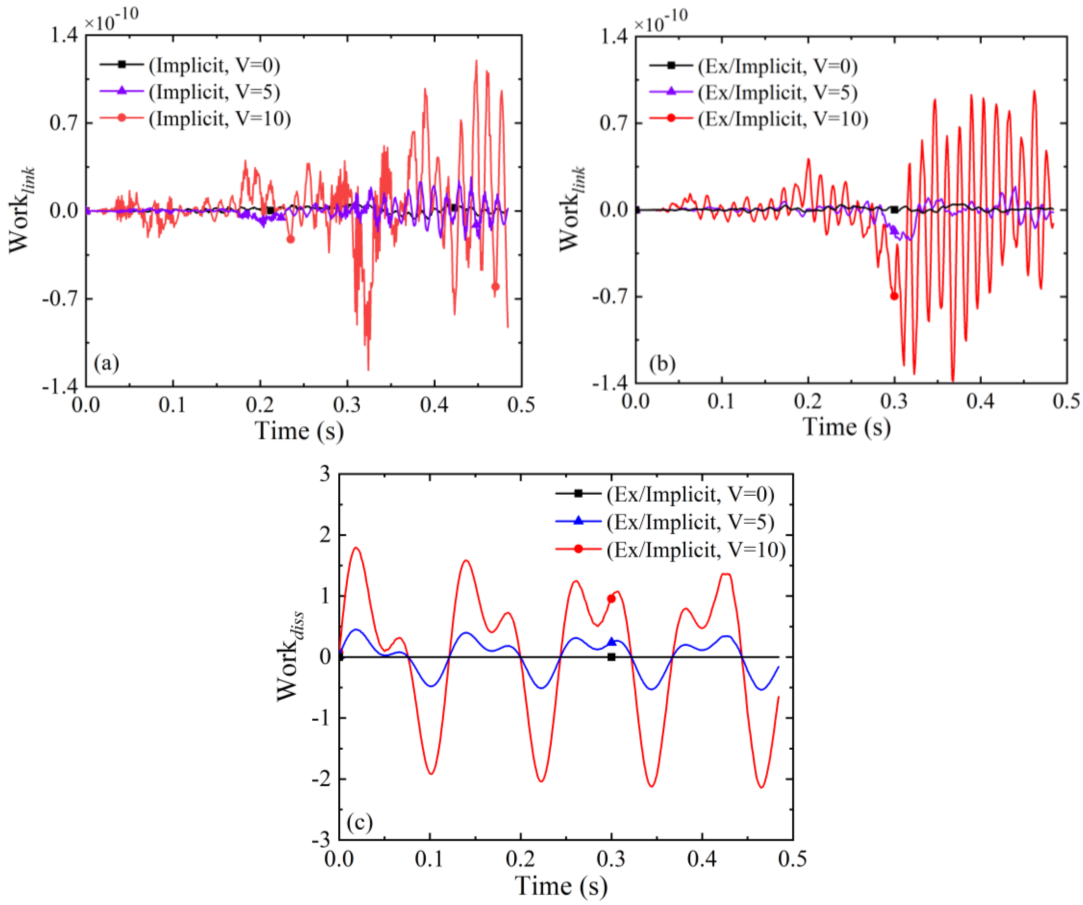

Fig. 7. The interface mechanical energy of the partitioned system. (a) the interface mechanical energy caused by link forces under Case I, (b) the interface mechanical energy caused by link forces under Case II, and (c) the algorithmic dissipation energy.

5.2 Discussion of accuracy

1) *Single-implicit integration scheme*

The single-implicit integration method with the same parameter combination in all subsystems (i.e., Case I) is used to solve the two models. For the partitioned model, two points exist at the same contact points (i.e., the upper subsystem has the up-points, and the lower subsystem has the down-points). However, the two points merge into a single contact point in the global model. Moreover, the wheel-rail contact points are time-variant so the global system matrix necessitates reassembly and recalculation at each time step [27]. Acceleration responses of the designated points are shown in Fig. 8.

For the front bogie $\boldsymbol{R}_1$ and the ballast-bridge interconnection points $\boldsymbol{R}_4$, which exhibit low-frequency vibration characteristics, the acceleration responses from the two models are completely identical. This is evident in Fig. 8(a) and (d). For the rail-sleeper interconnection points $\boldsymbol{R}_2$ and the sleeper-ballast interconnection points $\boldsymbol{R}_3$, which exhibit high-frequency vibration characteristics, the acceleration responses from the two models are identical, as shown in Figs. 8(b) and (c). The partially enlarged figure of $\boldsymbol{R}_2$, as depicted in Fig. 8(b), also reflects the observation in the highest frequency vibration domain. These observations suggest that results from the two models have the same amplitude decay and period elongation, which are the two accuracy indicators of integration methods. Namely, the proposed method has the same algorithm accuracy (second-order accuracy) as the Newmark method, including the amplitude decay and period elongation properties.

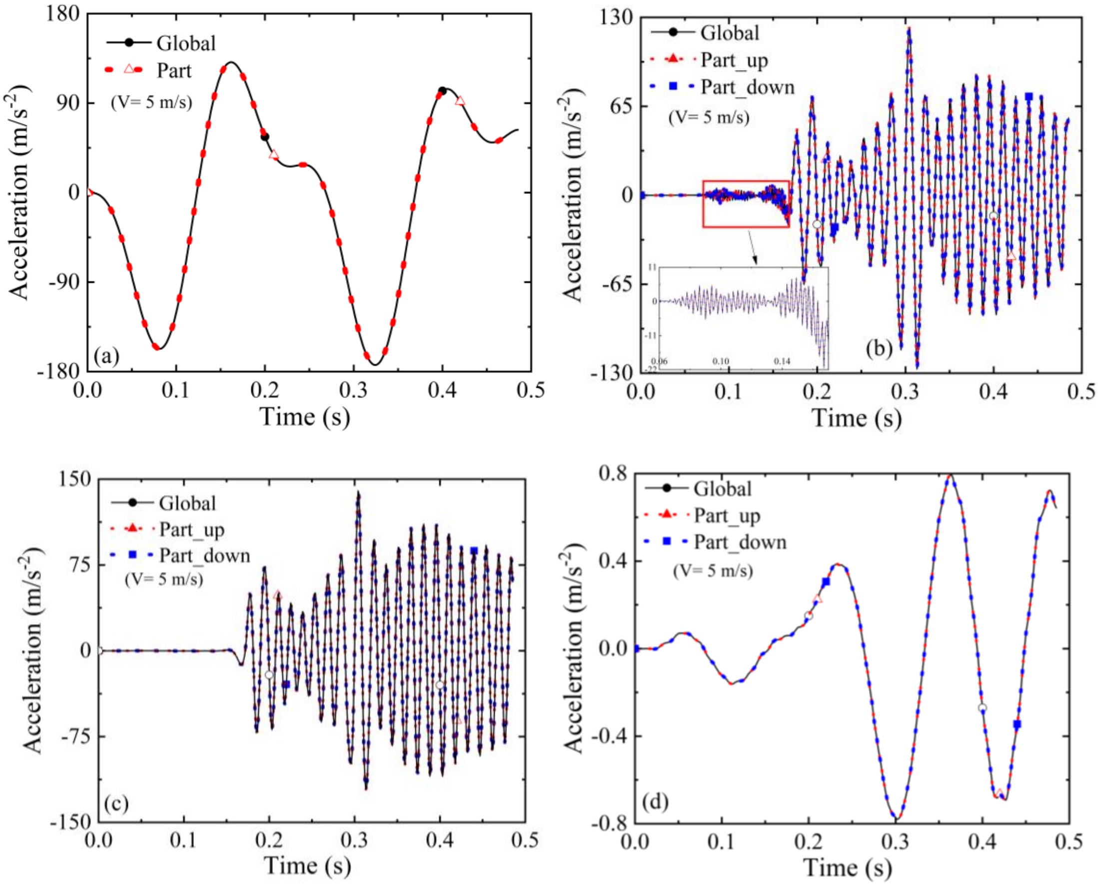

Fig. 8. Acceleration responses at the mid-span section of the bridge for the designated points: (a) the front bogie $\boldsymbol{R}_1$, (b) the rail-sleeper contact $\boldsymbol{R}_2$, (c) the sleeper-ballast contact $\boldsymbol{R}_3$, (d) the ballast-bridge contact $\boldsymbol{R}_4$. ‘Global’ stands for responses from the global model, ‘Part’ denotes responses from the partitioned model, and ‘up and down’ are, respectively, responses of the upper and bottom contact points of the partitioned model.

The acceleration responses of the time-variant wheel-rail contact points at the first wheelsets are presented in Fig. 9. The up-points from the vehicle subsystem are time-invariant, whereas the down-points belonging to the rail system are time-variant, which vary as the vehicle runs. Acceleration results of contact points show that the results of two points stay in touch, which suggests acceleration responses from the two points consistently overlap and align with the results from the global model. The enlarged view also supports this finding. Moreover, the results obtained from the global model exhibit second-order accuracy, and the results of both models are consistent. This implies that the proposed method ensures second-order accuracy as well.

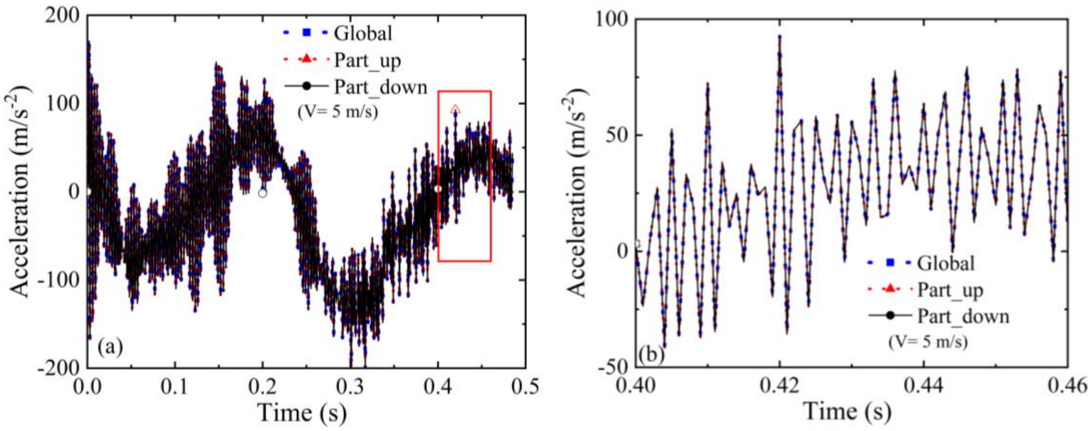

Fig. 9. Acceleration responses of (a) wheel-rail time-variant contact points at the first wheelset and (b) its partially enlarged figure from 0.4 s to 0.46 s.

2) *Explicit/implicit hybrid integration schemes*

The hybrid integration schemes combining explicit and implicit methods (i.e., Case II) are used in the computation for discussing the feasibility of hybrid computing. It is important to note that the global model employs a single implicit method with a unified parameter combination (γ = 1/2 and β = 1/4) for computing the entire system.

Although a relatively small time-step Δh = 0.001 s is employed to capture responses of the vehicle subsystem with low-frequency vibration property, a tiny difference in the bogie acceleration from the two models is still observed, which is marked in Fig. 10(a). This observation suggests that the proposed method allows for adjusting the accuracy of different subsystems by using respective parameters. Moreover, the highest vibration frequency of the vehicle system is 7.67 Hz, and Δ

h/T_{max} (i.e., the ratio of the time step size to the maximum period) equals 0.0077, which is far less than the threshold value of the Newmark explicit scheme (0.318) [38,41]. Hence, although the algorithmic parameter has a minor effect on the accuracy of the vehicle subsystem, the solved link forces at the vehicle-rail interconnected interfaces are still accurate, and the explicit integration scheme used in the vehicle subsystem can still capture vehicle responses accurately. The responses of other subsystems corroborate these findings, as shown in Figs. 10(b), (c), and (d). More specifically, for the low-frequency vibration points $\boldsymbol{R}_4$, the acceleration responses from the two models are completely consistent, as depicted in Fig. 10(d). For the high-frequency vibration points $\boldsymbol{R}_2$ and $\boldsymbol{R}_3$, the acceleration responses from the two models are the same, as shown in Figs. 10(b) and (c).

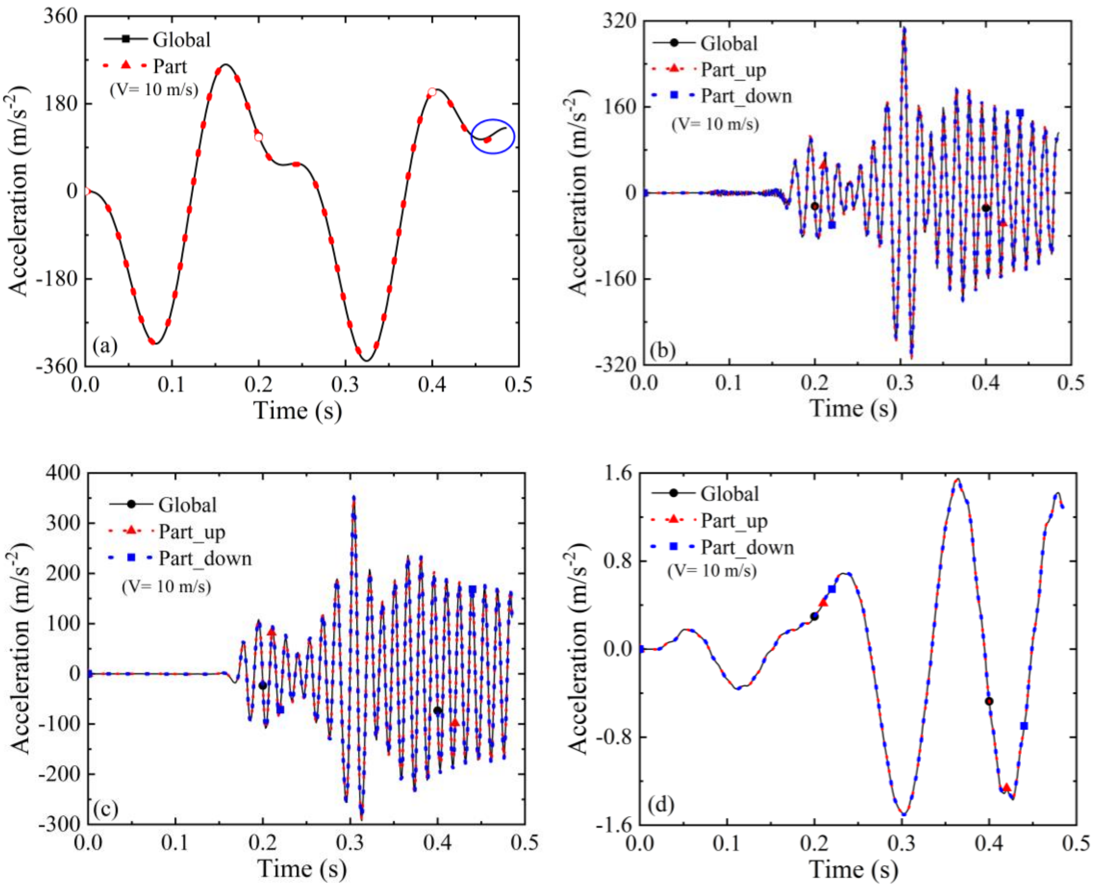

Fig. 10. Acceleration responses at the mid-span section of the bridge for the designated points: (a) the front bogie $\boldsymbol{R}_1$, (b) the rail-sleeper contact $\boldsymbol{R}_2$, (c) the sleeper-ballast contact $\boldsymbol{R}_3$, (d) the ballast-bridge contact $\boldsymbol{R}_4$.

The acceleration responses of the wheel-rail time-variant contact points at the first wheelsets are presented in Fig. 11. To observe responses from the two models, the responses from 0.4 s to 0.46 s are enlarged. It is shown that acceleration responses from the two models almost overlap. However, due to the explicit integration used in the vehicle subsystem, a slight difference is still captured at the peak value of the responses, as marked in Fig. 11(b). This finding suggests that the accuracy of different subsystems for the proposed method can be fine-tuned by using their parameters, and different integration schemes can be used in different subsystem computations.

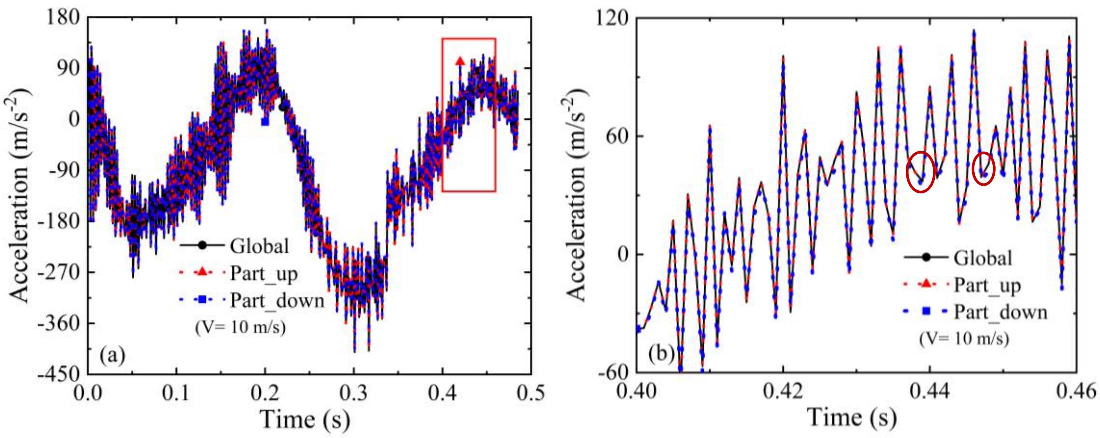

Fig. 11. Acceleration responses of (a) wheel-rail time-variant contact points at the first wheelset and (b) its partially enlarged figure from 0.4 s to 0.46 s.

3) *Discussion considering damping and irregularities*

A more realistic scenario for VRBS is calculated here by considering system damping and rail irregularities, where time-domain waves of irregularities can be found in [42], and the wheel-rail loadings caused by irregularity waves are calculated by the Hertzian spring stiffness (k_0) multiplied by time-domain waves. For simplification, the same Rayleigh damping coefficients (c_m = 1.2267 and c_k = 0.001309) are employed in all subsystem calculations. It is note that the Rayleigh coefficients only impact the formation of the damping matrix and do not affect the derivation of the proposed method. The explicit/implicit hybrid integration scheme is used in the computation. The acceleration responses of the designated points are presented in Fig. 12. It is shown that acceleration responses from the two models at the designated four points exhibit complete consistency, and this observation is consistent with Fig. 10. This finding indicates the feasibility of the hybrid integration scheme in partitioned computations and its ability to independently calculate subsystem responses. All subsystem responses maintain second-order accuracy.

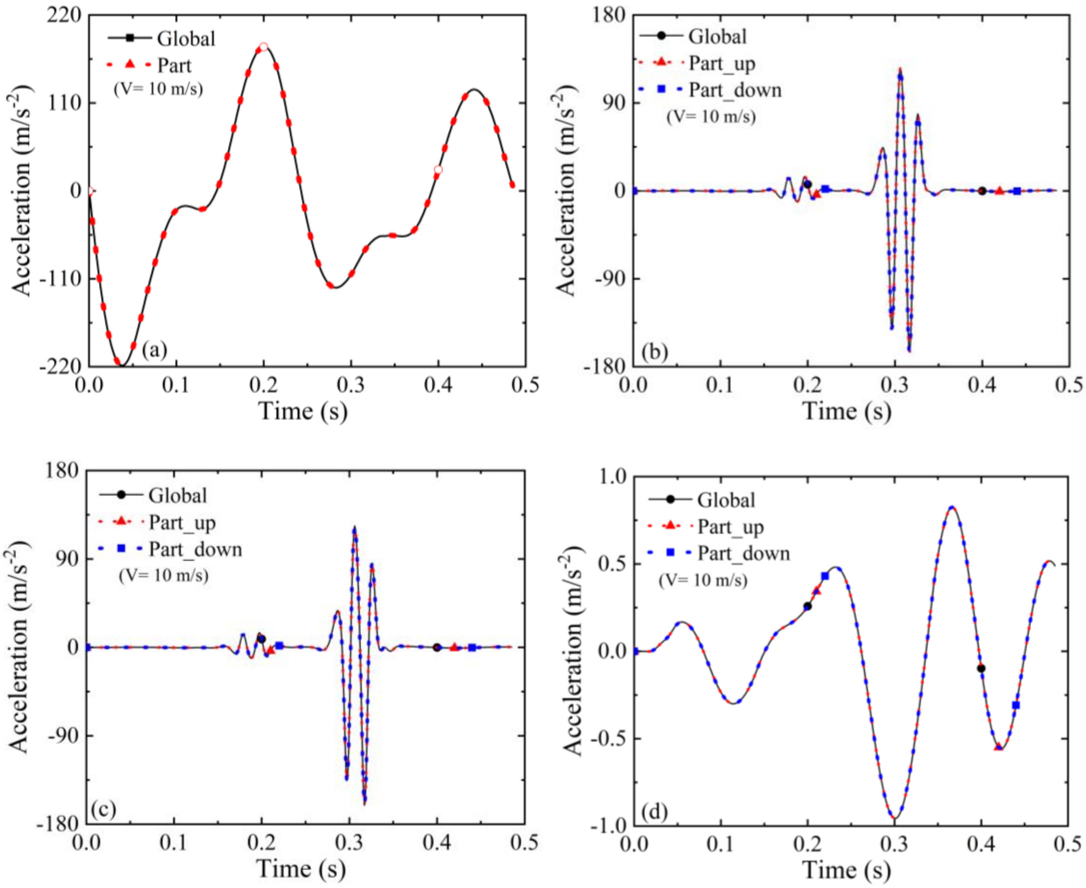

Fig. 12. Acceleration responses at the mid-span section of the bridge for the designated points: (a) the front bogie $\boldsymbol{R}_1$, (b) the rail-sleeper contact $\boldsymbol{R}_2$, (c) the sleeper-ballast contact $\boldsymbol{R}_3$, (d) the ballast-bridge contact $\boldsymbol{R}_4$.

The acceleration responses of time-variant wheel-rail contact points at the first wheelsets are presented in Fig. 13. The acceleration results demonstrate that the responses of the two points remain in contact and consistently align with the global model. The enlarged view provides additional support for this observation. Furthermore, the global model results exhibit second-order accuracy, and the consistency between the two models implies that second-order accuracy is also guaranteed in the proposed method.

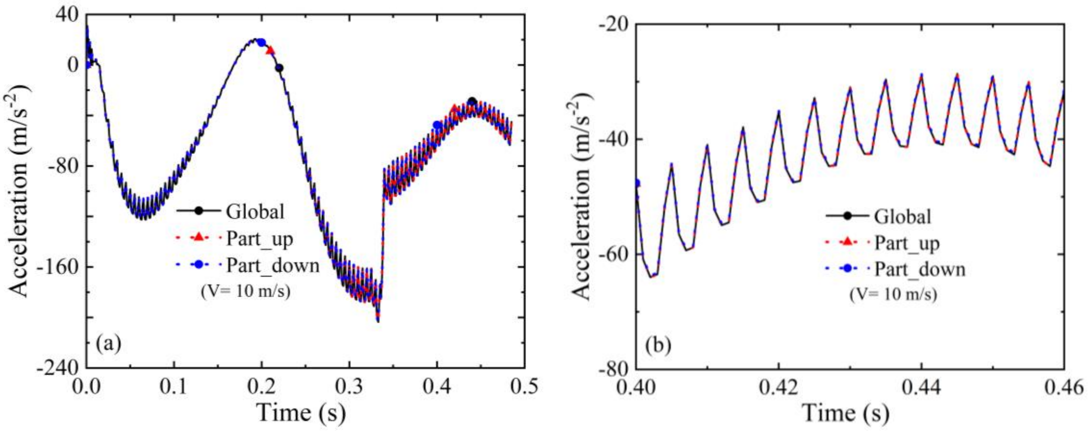

Fig. 13. Acceleration responses of (a) wheel-rail time-variant contact points at the first wheelset and (b) its partially enlarged figure from 0.4 s to 0.46 s.

5.3 Evaluation of efficiency

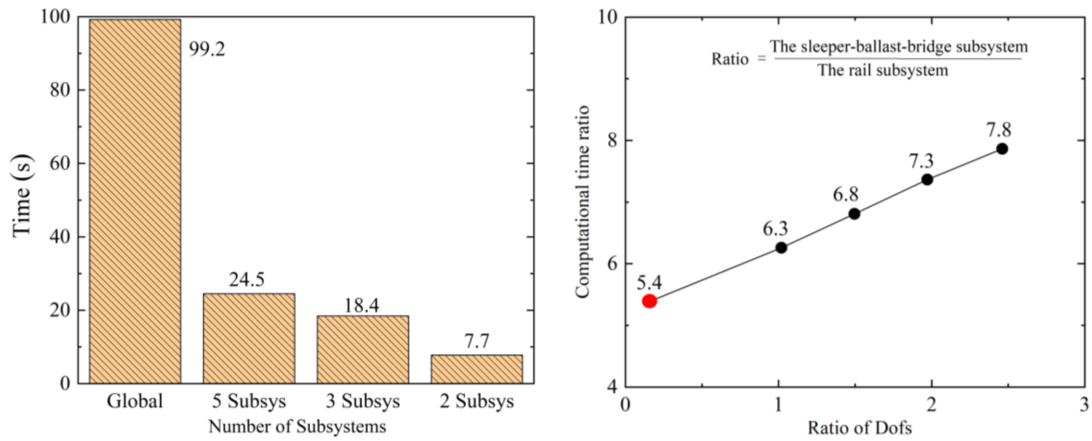

Fig. 14. Comparison of computational efficiency between the global model and the partitioned models (a) with 5, 3, and 2 subsystems and (b) with different ratios of the sleeper-ballast-bridge subsystem to the rail subsystem.

Considering the complexity of dynamic systems, different numbers of subsystems may be necessary in dynamic computations, two new partitioned manners are thus established in a similar manner for comparatively analyzing the computational time of different models, as presented in Fig. 14(a). More specifically, the three-subsystem model and the two-subsystem model. The three-subsystem model includes the vehicle subsystem, the rail subsystem with 2015 DOFs, and the sleeper-ballast-bridge subsystem with 322 DOFs, as shown in Fig. 5. The two-subsystem model consists of the vehicle subsystem and the rail-sleeper-ballast-bridge subsystem with 2272 DOFs, and corresponding system equations are given in Appendix C. Computational information follows Section 5.1, such as a constant speed of v_0 = 100 m/s, a time-step size of Δh = 0.001 s, and the total calculation time is 0.48 s. Due to the time-variant nature of rail-wheel contact points during vehicle operation, the global model [27] requires time-consuming reassembling and recomputing a new vehicle-rail-sleeper-ballast-bridge matrix at each time step. The computational time for the global model is thus the highest compared with those of the partitioned models, as shown in Fig. 14(a). Furthermore, in the partitioned model with five subsystems, since four-link forces exist in four interfaces, four linear equations (i.e., Eqs. (22), (24), (26), and (28)) need to be solved to obtain the four-link forces at each time step. Consequently, the analysis of link forces in the partitioned system involves more matrix computations than in the case of two or three subsystems. For the partitioned system with two subsystems, only one link force exists in the interface, as shown in Eq. (II-3). Consequently, the interface solver requires only one matrix operation to compute the link force. After obtaining the link force, the large time-variant system is divided into two relatively small time-invariant subsystems, facilitating efficient calculations. The partitioned model with two subsystems has thus the highest computational efficiency, approximately 11.9 times greater than that of the global model.

In addition, according to the three-subsystem model information, we know that the ratio of DOFs between the sleeper-ballast-bridge subsystem and the rail subsystem is around 0.16 (i.e., 322/2015). To further explore the computational efficiency of the proposed method under different DOF ratios of the two subsystems (i.e., the sleeper-ballast-bridge subsystem and the rail subsystem), the computing time ratio of the three-subsystem model and the entire model is investigated by increasing the ratio of DOFs in the sleeper-ballast-bridge subsystem. The result in Fig. 14(b) shows that the computational time ratios of the two models (i.e., the three-subsystem model and the entire model) increase with the increasing ratios of the sleeper-ballast-bridge subsystem and the rail subsystem. In other words, for complex and large systems, the superiority of the proposed method in terms of the computational efficiency is more evident. Therefore, the proposed method significantly enhances the computational efficiency.

6 Conclusions

In this study, a non-iterative partitioned computational method with the energy conservation property is proposed to calculate a large class of multi-subsystem time-variant dynamic systems. The proposed method addresses the problem that the partitioned time-variant system requires iterative computation and it implements a modular solution of time-variant systems. The theoretical demonstration and the accuracy and efficiency evaluation of the proposed method are performed by using a representative example, i.e., a vehicle-rail-sleeper-ballast system, comparing the results obtained from the global model [27]. The major contributions of this study are:

1) The proposed method implements a modular solution of time-variant systems; the high-order global system is divided into multiple reduced-order subsystems; and information exchange between the subsystems takes place only at the interface solver.
2) The proposed method decomposes a time-variant dynamic system into several independent time-invariant dynamic subsystems (≥ 3); the integration scheme, accuracy, and stability of each subsystem can be determined via its respective integration parameters; and the energy conservation property is ensured in the entire partitioned calculation process.
3) The proposed method addresses the problem of iterative computation for partitioned time-variant systems. It eliminates the need for time-variant matrices and complex iterative procedures, resulting in improved computational efficiency for partitioned computations.
4) For a two-subsystem time-variant dynamic system, the interface solver calculates only the link force through a single matrix operation, and the computational form is straightforward, resulting in a computational efficiency 12.9 times higher than that of the global model. The superiority of the proposed method in terms of the computational efficiency is more evident with the increasing ratios of time-invariant subsystems.

The developed method will be further extended to the multi-temporary calculation of a time-variant dynamic system using a 3-D VRBS considering the wheel-rail dynamic contacting in future work.

Acknowledgments

The study has been supported by the Young Scientists Fund of the National Natural Science Foundation of China (grant no. 52208212). The support is gratefully acknowledged. The opinions and conclusions presented in this paper are those of the authors and do not necessarily reflect the views of the sponsoring organizations.

Appendix A. Establishment of the vehicle-rail-bridge interaction system

A1.1 The vehicle subsystem

According to the assumptions in Section 2.1 and the relative motion of interconnected rigid bodies, the link forces marked in Fig. 2 can be derived as follows:

$$F_{ztkO_i} = k_{tz}\left[Z_c - Z_{t_i} - (-1)^{i+1} l_c \beta_c\right] \qquad (i=1,2) \tag{I-1}$$

$$F_{ztcO_i} = c_{tz}\left[\dot{Z}_c - \dot{Z}_{t_i} - (-1)^{i+1} l_c \dot{\beta}_c\right] \qquad (i=1,2) \tag{I-2}$$

$$F_{xtkO_i} = k_{tx}\left[H_{cb}\beta_c + H_{bt}\beta_{t_i}\right] \qquad (i=1,2) \tag{I-3}$$

$$F_{xtcO_i} = c_{tx}\left[H_{cb}\dot{\beta}_c + H_{bt}\dot{\beta}_{t_i}\right] \qquad (i=1,2) \tag{I-4}$$

$$F_{zfkO_i} = k_{pz}\left[Z_{tj} - Z_{wi} - (-1)^{i+1} l_t \beta_{tj}\right] \left(i=1,2,3,4 \quad j=\frac{2i+1+(-1)^{i+1}}{4} \right) \tag{I-5}$$

$$F_{zfcO_i} = c_{pz}\left[\dot{Z}_{tj} - \dot{Z}_{wi} - (-1)^{i+1} l_t \dot{\beta}_{tj}\right] \left(i=1,2,3,4 \quad j=\frac{2i+1+(-1)^{i+1}}{4} \right) \tag{I-6}$$

where the subscript O = (L, R) stands for the force orientations including L and R (similarly hereinafter); the force directions are stipulated in Fig. 2; and the dot on symbols is the derivative with respect to time. Based on the obtained forces in Eqs. (I-1) ~ (I-6), the governing equations of the ten-DOF vehicle are derived as:

$$M_c \ddot{Z}_c = M_c g - \sum_{i=1}^{2} F_{ztdO_i} \tag{I-7}$$

$$I_{cy}\ddot{\beta}_c = \sum_{i=1}^{2}\left(\left(-1\right)^{i+1} l_c F_{ztdO_i} - H_{cb}\left(F_{xtdO_i} + F_{xsO_i}\right)\right) \tag{I-8}$$

$$M_t \ddot{Z}_{t_1} = M_t g + F_{ztdO_1} - \sum_{i=1}^{2}\left(F_{zfdO_i}\right) \tag{I-9}$$

$$I_{ty}\ddot{\beta}_{t_1} = -H_{bt}\left(F_{xtdO_1} + F_{xsO_1}\right) + \sum_{i=1}^{2}\left(\left(-1\right)^{i+1} l_t F_{zfdO_i} - H_{tw} F_{xfdO_i}\right) \tag{I-10}$$

$$M_t \ddot{Z}_{t_2} = M_t g + F_{ztdO_2} - \sum_{i=3}^{4} F_{zfdO_i} \tag{I-11}$$

$$I_{ty}\ddot{\beta}_{t_2} = -H_{bt}\left(F_{xtdO_2} + F_{xsO_2}\right) + \sum_{i=3}^{4}\left(\left(-1\right)^{i+1} l_t F_{zfdO_i} - H_{tw} F_{xfdO_i}\right) \tag{I-12}$$

$$M_w \ddot{Z}_{wi} = P_i = M_w g + \sum_{i=1}^{4}\left(F_{zfdOi} - N_{Ozi} - F_{Ozi}\right) \quad \left(i = 1 \ldots 4\right) \tag{I-13}$$

where the subscript d = (c, k) stands for the force types including damping forces (c) and spring forces (k). The types and orientations of forces should be added to the corresponding equations. Substituting the link forces into the motion of equations, the governing equation of the vehicle subsystem is written in the matrix form as follows:

$$\mathbf{M}_V \Delta\ddot{\mathbf{U}}_V + \mathbf{C}_V \Delta\dot{\mathbf{U}}_V + \mathbf{K}_V \Delta\mathbf{U}_V + \left(\boldsymbol{L}_1^{W\bullet R}\right)^T \Delta\mathbf{P}_{VR} = \Delta\mathbf{P}_{VE} + \Delta\mathbf{Fv} \tag{I-14a}$$

$$\Delta\mathbf{Fv} = \left(\boldsymbol{L}_1^{W\bullet R}\right)^T \left(\boldsymbol{L}_{1t_{i+1}}^{R\bullet W} - \boldsymbol{L}_{1t_i}^{R\bullet W}\right) \mathbf{U}_{(R,t_i)} k_0 + \left(\boldsymbol{L}_1^{W\bullet R}\right)^T \left(\boldsymbol{L}_{1t_{i+1}}^{R\bullet W} - \boldsymbol{L}_{1t_i}^{R\bullet W}\right) \dot{\mathbf{U}}_{(R,t_i)} c_0 \tag{I-14b}$$

where $\mathbf{M}_V$, $\mathbf{K}_V$, and $\mathbf{C}_V$ are, respectively, the mass matrix, stiffness matrix, and damping matrix of the vehicle (See Eqs. (I-15)); and $\Delta\mathbf{P}_{VR}$, $\Delta\mathbf{P}_{VE}$, and $\Delta\mathbf{F}_V$ refer to the link force to be solved, the external force, and the time-variant loads caused by the vehicle running, respectively. The shared nodes for the wheel and rail are set on the rail, as shown in Figs. 3 and 4.

$$\boldsymbol{M}_V = \begin{bmatrix} M_c & I_{cy} & M_t & I_{ty} & M_t & I_{ty} & M_w & M_w & M_w & M_w \end{bmatrix}^T \tag{I-15a}$$

$$\boldsymbol{K}_V = \begin{bmatrix} 4k_{tz} & & -2k_{tz} & & -2k_{tz} & & & & & \\ & K_{22} & 2l_c k_{tz} & K_{24} & -2l_c k_{tz} & K_{26} & & & & \\ & & K_{33} & & & & -2k_{pz} & -2k_{pz} & & \\ & & & K_{44} & & & 2l_t k_{pz} & -2l_t k_{pz} & & \\ & & & & K_{55} & & & & -2k_{pz} & -2k_{pz} \\ & & & & & K_{66} & & & 2l_t k_{pz} & -2l_t k_{pz} \\ & & \mathit{Symmetric} & & & & 2k_{pz} & & & \\ & & & & & & & 2k_{pz} & & \\ & & & & & & & & 2k_{pz} & \\ & & & & & & & & & 2k_{pz} \end{bmatrix} \tag{I-15b}$$

$$K_{22} = 4\left(H_{cb}^2 k_{tx} + l_c^2 k_{tz}\right),\ K_{24} = 2H_{cb}H_{bt}k_{tx},\ K_{26} = 2H_{cb}H_{bt}k_{tx},\ K_{33} = 2\left(k_{tz} + 2k_{pz}\right)$$

$$K_{44} = 2\left(2l_t^2 k_{pz} + 2H_{tw}^2 k_{px} + H_{bt}^2 k_{tx}\right), K_{55} = 2\left(k_{tz} + 2k_{pz}\right)$$

$$K_{66} = 2\left(2l_t^2 k_{pz} + 2H_{tw}^2 k_{px} + H_{bt}^2 k_{tx}\right)$$

$$\Delta \boldsymbol{P}_{VE} = \begin{bmatrix} M_c g & 0 & M_t g & 0 & M_t g & 0 & P_1 & P_2 & P_3 & P_4 \end{bmatrix}^T \tag{I-15c}$$

A1.2 The rail subsystem

Similarly, for the **rail** subsystem, according to the relative motion of the rail and the ith sleeper (x_i), the vertical forces of the right-side rail, as marked in Fig. 3(b), are calculated as follows:

$$F_{v_{1i}} = k_{pv}\left[Z_{Rr}(x_i) - Z_s(x_i)\right] + C_{pv}\left[\dot{Z}_{Rr}(x_i) - \dot{Z}_s(x_i)\right] \tag{I-16}$$

$$F_{v_{2i}} = k_{pv}\left[Z_{Rr}(x_i) - Z_s(x_i)\right] + C_{pv}\left[\dot{Z}_{Rr}(x_i) - \dot{Z}_s(x_i)\right] \tag{I-17}$$

where the first subscript of the kinematic quantity Z represents the subsystem name (r = rail, s = sleeper) if the orientation symbol (i.e., R/L) does not exist. Only the vertical forces at the right-side rail are presented. Substituting the link forces into the motion of equations of the rail, one has:

$$\mathbf{M}_R \Delta\ddot{\mathbf{U}}_R + \mathbf{C}_R \Delta\dot{\mathbf{U}}_R + \mathbf{K}_R \Delta\mathbf{U}_R + \left(\boldsymbol{L}_{1t_{i+1}}^{R\bullet W}\right)^T \Delta\mathbf{P}_{VR} + \left(\boldsymbol{L}_2^{R\bullet S}\right)^T \Delta\mathbf{P}_{RS} = \Delta\mathbf{P}_{RE} + \Delta\mathbf{Fr} \tag{I-18a}$$

$$\begin{aligned} \Delta\mathbf{Fr} = & -\left(\boldsymbol{L}_{1t_i}^{R\bullet W}\right)^T \left(\boldsymbol{L}_{1t_i}^{R\bullet W}\mathbf{U}_{(R,t_i)} - \boldsymbol{L}_0^{W\bullet R}\mathbf{U}_{(V,t_i)}\right)k_0 + \left(\boldsymbol{L}_{1t_{i+1}}^{R\bullet W}\right)^T \left(\boldsymbol{L}_0^{W\bullet R}\mathbf{U}_{(V,t_i)} - \boldsymbol{L}_{1t_{i+1}}^{R\bullet W}\mathbf{U}_{(R,t_i)}\right)k_0 \\ & -\left(\boldsymbol{L}_{1t_i}^{R\bullet W}\right)^T \left(\boldsymbol{L}_{1t_i}^{R\bullet W}\dot{\mathbf{U}}_{(R,t_i)} - \boldsymbol{L}_0^{W\bullet R}\dot{\mathbf{U}}_{(V,t_i)}\right)c_0 + \left(\boldsymbol{L}_{1t_{i+1}}^{R\bullet W}\right)^T \left(\boldsymbol{L}_0^{W\bullet R}\dot{\mathbf{U}}_{(V,t_i)} - \boldsymbol{L}_{1t_{i+1}}^{R\bullet W}\dot{\mathbf{U}}_{(R,t_i)}\right)c_0 \end{aligned} \tag{I-18b}$$

$$\Delta\,\mathbf{P}_R = \left\{\ldots \quad \left[2k_{pv}Z_s(x_i) + 2C_{pv}\dot{Z}_s(x_i)\right] \quad \ldots \quad \left[P_1(x_1),\quad P_2(x_2),\quad P_3(x_3),\quad P_4(x_4)\right] \quad \ldots\right\} \tag{I-18c}$$

$$\mathbf{K}_R = \left(\mathbf{K}_{Ra} + \mathbf{K}_{Rs}\right) \qquad \mathbf{C}_R = \left(\mathbf{C}_{Ra} + \mathbf{C}_{Rs}\right) \tag{I-18d}$$

where $\mathbf{K}_R$ and $\mathbf{C}_R$ are, respectively, the coupling stiffness and damping matrices due to the interconnection of the rail and sleeper; $\Delta\mathbf{P}_{RS}$ and $\Delta\mathbf{P}_{RE}$ refer to the link forces from the vehicle subsystem and the rail external forces, respectively; and $\Delta\mathbf{F}_r$ refers to the time-variant loads caused by the vehicle running.

A1.3 The sleeper subsystem

For the **sleeper** subsystem, according to the relative motion of the rail, sleeper, and ballast, the vertical forces acted on the ith sleeper (x_i), as marked in Fig. 3(b), can be computed as follows:

$$F_{rvi}^{O} = 2k_{pv}\left[Z_{Or}(x_i) - Z_{si}(x_i)\right] + 2c_{pv}\left[\dot{Z}_{Or}(x_i) - \dot{Z}_{si}(x_i)\right] \tag{I-19}$$

$$F_{svi}^{O} = k_{bv}\left[Z_{s}(x_i) - Z_{Ob}(x_i)\right] + c_{bv}\left[\dot{Z}_{s}(x_i) - \dot{Z}_{Ob}(x_i)\right] \tag{I-20}$$

Substituting the link forces into the motion of the equation of rails, one has:

$$\begin{gathered} M_{si}\ddot{Z}_{si} + \begin{pmatrix} \left(4k_{pv} + 2k_{bv}\right)Z_{si} + \\ \left(4c_{pv} + 2c_{bv}\right)\dot{Z}_{si} \end{pmatrix} = P_{si} = \\ \begin{pmatrix} 2k_{pv}\left(Z_{Lr}(x_i) + Z_{Rr}(x_i)\right) + 2c_{pv}\left(\dot{Z}_{Lr}(x_i) + \dot{Z}_{Rr}(x_i)\right) \\ +k_{bv}\left(Z_{Lb}(x_i) + Z_{Rb}(x_i)\right) + c_{bv}\left(\dot{Z}_{Lb}(x_i) + \dot{Z}_{Rb}(x_i)\right) \end{pmatrix} \quad \left(i = 1, \ldots n_s\right) \end{gathered} \tag{I-21a}$$

$$\mathbf{M}_S\Delta\ddot{\mathbf{U}}_S + \mathbf{C}_S\Delta\dot{\mathbf{U}}_S + \mathbf{K}_S\Delta\mathbf{U}_S + \left(\boldsymbol{L}_2^{S\cdot R}\right)^T\Delta\mathbf{P}_{RS} + \left(\boldsymbol{L}_3^{S\cdot B}\right)^T\Delta\mathbf{P}_{SB} = \Delta\mathbf{P}_{SE} \tag{I-21b}$$

where M_{si}, Z_{si}, and Z_{bi} are, respectively, the mass of the ith sleeper, the vertical displacement of the sleeper and ballast, and $\Delta\mathbf{P}_{SB}$ and $\Delta\mathbf{P}_{SE}$ refer to the link forces from the ballast and the external force, respectively. Considering the number of sleepers and ballasts (n_s and n_b), the matrix form of the sleeper subsystem can be easily obtained.

A1.4 The ballast subsystem

For the **ballast** subsystem, the vertical forces applied to the ith ballast ($Z_{bi}^{R/L}$), as marked in Fig. 3(c), are calculated as follows:

$$F_{b2i}^{O} = k_{bw}\left[Z_{bi}^{O} - Z_{b(i-1)}^{O}\right] + c_{bw}\left[\dot{Z}_{bi}^{O} - \dot{Z}_{b(i-1)}^{O}\right] \tag{I-22}$$

$$F_{b1i}^{O} = k_{bw}\left[Z_{bi}^{O} - Z_{b(i+1)}^{O}\right] + c_{bw}\left[\dot{Z}_{bi}^{O} - \dot{Z}_{b(i+1)}^{O}\right] \tag{I-23}$$

$$F_{bLi}^{O} = k_{bw}\left[Z_{bi}^{O} - Z_{bi}^{-O} \right] + c_{bw}\left[\dot{Z}_{bi}^{O} - \dot{Z}_{Li}^{-O} \right] \tag{I-24}$$

$$F_{bfi}^{O} = k_{fv}\left(Z_{br} - Z_{bi}^{O} \right) + c_{fv}\left(\dot{Z}_{br} - \dot{Z}_{bi}^{O} \right) \tag{I-25}$$

$$F_{svi}^{O} = k_{bv}\left(Z_{si} - Z_{bi}^{O} \right) + c_{bv}\left(\dot{Z}_{si} - \dot{Z}_{bi}^{O} \right) \tag{I-26}$$

where the superscript -*O* denotes the opposite orientations to *O*, (i.e., if *O* = L, then -*O* = R). Z_{br} is the vertical displacement of the bridge. The vertical motion of the equation of the both-side ballast under the *i*th sleeper can be derived as follows:

$$M_b \ddot{Z}_{bi}^{O} = F_{svi}^{O} + F_{bfi}^{O} - F_{b1i}^{O} - F_{b2i}^{O} - F_{bLi}^{O} \tag{I-27}$$

where M_b is the mass of the *i*th ballast. Substituting the link forces into the motion of equations of the ballast, one has:

$$\begin{aligned} &M_b \ddot{Z}_{bi}^{O} + \left(3k_{bw} + k_{bv} + k_{fv} \right) Z_{bi}^{O} - k_{bw}\left[Z_{b(i-1)}^{O} + Z_{bi}^{-O} + Z_{b(i+1)}^{O} \right] \\ &\quad + \left(3c_{bw} + c_{bv} + c_{fv} \right) \dot{Z}_{bi}^{O} - c_{bw}\left[\dot{Z}_{b(i-1)}^{O} + \dot{Z}_{Li}^{-O} + \dot{Z}_{b(i+1)}^{O} \right] \\ &= P_{bi} = k_{bv} Z_{si} + c_{bv} \dot{Z}_{si} + k_{fv} Z_{br} + c_{fv} \dot{Z}_{br} \qquad \left(i = 1, \ldots n_b \right) \end{aligned} \tag{I-28a}$$

$$\mathbf{M}_B \Delta \ddot{\mathbf{U}}_B + \mathbf{C}_B \Delta \dot{\mathbf{U}}_B + \mathbf{K}_B \Delta \mathbf{U}_B + \left(\boldsymbol{L}_3^{B \bullet S} \right)^T \Delta \mathbf{P}_{SB} + \left(\boldsymbol{L}_4^{B \bullet Br} \right)^T \Delta \mathbf{P}_{B.Br} = \Delta \mathbf{P}_{BE} \tag{I-28b}$$

where M_b and P_{bi} are, respectively, the mass and loading of the ballast; Z_{br} is the vertical displacement of the bridge; and $\Delta\mathbf{P}_{B.Br}$ and $\Delta\mathbf{P}_{BE}$ refer to the link forces from the bridge and the external force, respectively. The stiffness and damping matrix of the sleeper subsystem are:

$$\mathbf{K}_{bw} = \begin{bmatrix} k_{bv} + 2k_w + k_{fv} & -k_w & & \\ -k_w & k_{bv} + 3k_w + k_{fv} & -k_w & \\ & \cdots & \cdots & -k_w \\ & & -k_w & k_{bv} + 2k_w + k_{fv} \end{bmatrix}_{n_b \times n_b} \tag{I-29}$$

$$\mathbf{C}_{bw} = \begin{bmatrix} c_{bv} + 3c_w + c_{fv} & -c_w & & \\ -c_w & c_{bv} + 3c_w + c_{fv} & -c_w & \\ & \cdots & \cdots & -c_w \\ & & -c_w & c_{bv} + 3c_w + c_{fv} \end{bmatrix}_{n_b \times n_b} \tag{I-34}$$

The ballast boundary conditions at the starting and ending positions are:

$$\begin{cases} Z^{O}_{b_0} = \dot{Z}^{O}_{b_0} = 0 \\ Z^{O}_{b_{(N+1)}} = \dot{Z}^{O}_{b_{(N+1)}} = 0 \end{cases} \tag{I-31}$$

A1.5 The bridge subsystem

For the **bridge** subsystem, the governing equation is:

$$\mathbf{M}_{Br}\Delta\ddot{\mathbf{U}}_{Br} + \mathbf{C}_{Br}\Delta\dot{\mathbf{U}}_{Br} + \mathbf{K}_{Br}\Delta\mathbf{U}_{Br} + \left(\boldsymbol{L}_4^{Br\bullet B}\right)^T \Delta\mathbf{P}_{B.Br} = \Delta\mathbf{P}_{BrE} \tag{I-32a}$$

where $\Delta\boldsymbol{P}_{BrE}$ is the external forces applied to the bridge deck; and $\Delta\boldsymbol{P}_{B.Br}$ to be solved is the link force at the fourth interface.

Appendix B. The computational procedure of the partitioned system

Table 1. Computational flowchart

***Multi-partitioned structural analyzers*:**

(1) Calculate relative matrices and vectors

$$\boldsymbol{K}_k, \boldsymbol{C}_k, \boldsymbol{M}_k, \boldsymbol{K}_k^*, \boldsymbol{L}_l^{k\bullet j^T}, \boldsymbol{U}_{t_0}^k, \dot{\boldsymbol{U}}_{t_0}^k, \ddot{\boldsymbol{U}}_{t_0}^k \quad (\mathrm{k} = V, R, S, B, Br)$$

(See Eqs. (1) ~ (5))

(2) Calculate constant matrices

$$\boldsymbol{G}_{W\bullet S}, \boldsymbol{G}_{S\bullet W}, \boldsymbol{G}_{R\bullet B}, \boldsymbol{G}_{B\bullet R}, \boldsymbol{G}_{S\bullet Br}, \boldsymbol{G}_{Br\bullet S}, \boldsymbol{H}_{V\bullet R}, \boldsymbol{H}_{R\bullet S}, \boldsymbol{H}_{S\bullet B}, \boldsymbol{H}_{B\bullet Br}$$

(See Eqs. (23bc), (25bcd), (27bcd), and (29bcd))

(3) Calculate the velocity increments

$$\Delta\dot{\boldsymbol{U}}_{VR}^{Ext}, \Delta\dot{\boldsymbol{U}}_{RS}^{Ext}, \Delta\dot{\boldsymbol{U}}_{SB}^{Ext}, \Delta\dot{\boldsymbol{U}}_{BBr}^{Ext}$$

(See Eqs. (23a), (25a), (27a), and (29a))

(4) Calculate link forces

$$\Delta\boldsymbol{P}_{(VR,t_{i+1})}, \Delta\boldsymbol{P}_{(RS,t_{i+1})}, \Delta\boldsymbol{P}_{(SB,t_{i+1})}, \Delta\boldsymbol{P}_{(BBr,t_{i+1})}$$

(See Eqs. (22), (24), (26), and (28))

***The interface solver*:**

(5) Calculate responses of all subsystems

(See Eq. (15))

(6) Return to (3) for the next step or stop

Appendix C. Two subsystems for VRBS.

The entire system is here divided into two subsystems (as shown in Fig. A1), i.e., the vehicle subsystem ($\square_V$) (i.e., Fig. A1 (a)) and the rail-sleeper-ballast-bridge subsystem ($\square_{RB}$) (i.e., Fig. A1 (c)). Referring to Appendix A, the dynamic governing equations of the two subsystems are similarly derived as follows:

$$\mathbf{M}_V\Delta\ddot{\mathbf{U}}_{(V,t_{i+1})}+\mathbf{C}_V\Delta\dot{\mathbf{U}}_{(V,t_{i+1})}+\mathbf{K}_V\Delta\mathbf{U}_{(V,t_{i+1})}+\left(\boldsymbol{L}_1^{W\bullet R}\right)^T\Delta\boldsymbol{P}_{(VRB,t_{i+1})}=\Delta\mathbf{P}_{VE}+\Delta\mathbf{Fv} \tag{II-1}$$

$$\mathbf{M}_{RB}\Delta\ddot{\mathbf{U}}_{(RB,t_{i+1})}+\mathbf{C}_{RB}\Delta\dot{\mathbf{U}}_{(RB,t_{i+1})}+\mathbf{K}_{RB}\Delta\mathbf{U}_{(RB,t_{i+1})}+\left(\boldsymbol{L}_{1t_{i+1}}^{RB\bullet W}\right)^T\Delta\boldsymbol{P}_{(VRB,t_{i+1})}=\Delta\mathbf{P}_{RBE}+\Delta\mathbf{Fr} \tag{II-2}$$

where the subscript RB stands for the rail-sleeper-ballast-bridge subsystem; Eq. (II-1) is identical to Eq. (I-14a); and the corresponding matrices and vectors can be obtained similarly. Only one interface (Similar to Eq. (6)) exists in the two-subdomain system. Based on the Newmark scheme (i.e., Eq. (18)) and the velocity continuity conditions (Similar to Eq. (19)), the only unknown link force (i.e., link forces $\triangle\boldsymbol{P}_{(VRB,\,t_{i+1})}$) is solved as follows:

$$\begin{aligned}&\boldsymbol{L}_1^{W\bullet RB}\Delta\dot{\boldsymbol{U}}_{(VE,t_{i+1})}^{Ext}+\boldsymbol{L}_{1t_{i+1}}^{RB\bullet W}\Delta\dot{\boldsymbol{U}}_{(RBE,t_{i+1})}^{Ext}=\\&\left(\boldsymbol{L}_1^{W\bullet RB}\boldsymbol{K}_V^{*-1}\left(\boldsymbol{L}_1^{W\bullet RB}\right)^T+\boldsymbol{L}_{1t_{i+1}}^{RB\bullet W}\boldsymbol{K}_{RB}^{*-1}\left(\boldsymbol{L}_{1t_{i+1}}^{RB\bullet W}\right)^T\right)\Delta\boldsymbol{P}_{(VRB,t_{i+1})}\end{aligned} \tag{II-3}$$

All coefficients in Eq. (II-3) are constant for a linear system, and the only link force can be computed via Eq. (II-3). After getting the link forces, the partitioned system responses are calculated via the Newmark method (Similar to Eq. (14)).

To present the method more directly, a two-subsystem model considering the spring-mass subsystem and the continuous beam subsystem is built in Fig. A2, the corresponding governing equation can be written as follows:

$$m_S\Delta\ddot{\boldsymbol{U}}_{(S,t_{i+1})}+c_S\Delta\dot{\boldsymbol{U}}_{(S,t_{i+1})}+k_S\Delta\boldsymbol{U}_{(S,t_{i+1})}+[0\quad 1]^T\Delta P_{(SB,t_{i+1})}=\Delta\boldsymbol{P}_{SE}+\Delta\boldsymbol{Fv} \tag{II-4a}$$

$$\boldsymbol{M}_B\Delta\ddot{\boldsymbol{U}}_{(B,t_{i+1})}+\boldsymbol{C}_B\Delta\dot{\boldsymbol{U}}_{(B,t_{i+1})}+\boldsymbol{K}_B\Delta\boldsymbol{U}_{(B,t_{i+1})}+\left(\boldsymbol{L}_{1t_{i+1}}^{B\bullet W}\right)^T\Delta\boldsymbol{P}_{(SB,t_{i+1})}=\Delta\boldsymbol{P}_{BE}+\Delta\boldsymbol{Fr} \tag{II-4b}$$

$$\Delta\boldsymbol{Fv}=[0\quad 1]^T\left(\boldsymbol{L}_{1t_{i+1}}^{RB\bullet W}-\boldsymbol{L}_{1t_i}^{RB\bullet W}\right)\boldsymbol{U}_{(B,t_i)}k_s \tag{II-4c}$$

$$\Delta \boldsymbol{Fr}=\begin{pmatrix} \left(\boldsymbol{L}_{1t_{i+1}}^{B\bullet S}\right)^T \left(\begin{bmatrix}0 & 1\end{bmatrix}\boldsymbol{U}_{(S,t_i)} - \boldsymbol{L}_{1t_{i+1}}^{B\bullet S}\boldsymbol{U}_{(B,t_i)}\right) - \\ \left(\boldsymbol{L}_{1t_i}^{B\bullet S}\right)^T \left(\boldsymbol{L}_{1t_i}^{B\bullet S}\boldsymbol{U}_{(B,t_i)} - \begin{bmatrix}0 & 1\end{bmatrix}\boldsymbol{U}_{(S,t_i)}\right) \end{pmatrix} k_0 \qquad \text{(II-4d)}$$

where m_a, c_a, k_a, $\Delta\boldsymbol{U}_a$, $\Delta\dot{\boldsymbol{U}}_a$, $\Delta\ddot{\boldsymbol{U}}_a$, and $\Delta\boldsymbol{P}_{aE}$ are, respectively, the mass, damping, stiffness, displacement, velocity, acceleration, and external forces of the subsystem. They represent the parameters of the spring-mass subsystem and the continuous beam subsystem when $a = S$ and $a = B$, respectively. Only one link force (i.e., $\Delta P_{(SB,t_{i+1})}$) exists in the two-subdomain system, and it can be solved at each time step by using the following simplified equation (II-3). This step corresponds to (4) in Table 1.

$$\begin{bmatrix}0 & 1\end{bmatrix}\Delta\dot{\boldsymbol{U}}_{(SE,t_{i+1})}^{Ext} + \boldsymbol{L}_{1t_{i+1}}^{B\bullet S}\Delta\dot{\boldsymbol{U}}_{(BE,t_{i+1})}^{Ext} = \left(\begin{bmatrix}0 & 1\end{bmatrix}\boldsymbol{K}_S^{*-1}\begin{bmatrix}0 & 1\end{bmatrix}^T + \boldsymbol{L}_{1t_{i+1}}^{B\bullet S}\boldsymbol{K}_B^{*-1}\left(\boldsymbol{L}_{1t_{i+1}}^{B\bullet S}\right)^T\right)\Delta P_{(SB,t_{i+1})} \qquad \text{(II-5)}$$

where $\Delta\dot{\boldsymbol{U}}_{(SE,t_{i+1})}^{Ext}$ *and* $\Delta\dot{\boldsymbol{U}}_{(RBE,t_{i+1})}^{Ext}$ are, respectively, velocity increasements of the two subsystems caused by the external forces, which can be calculated by using Eq. (18), corresponding to (3) in Table 1. $\boldsymbol{K}_S^{*-1}$ *and* $\boldsymbol{K}_B^{*-1}$ are, respectively, equivalent stiffness matrices of the spring-mass subsystem and the continuous beam subsystem, which can be solved using Eq. (12). After obtaining the link force ΔP_{SB}, all responses can be calculated by using Eq. (II-4). This step corresponds to (5) in Table 1. Based on the two-subsystem model, the sensitivity analysis with respect to stiffness of the partition is performed by using the calculational information in Fig. A2. The results show that the connections between partitions do not influence the results.

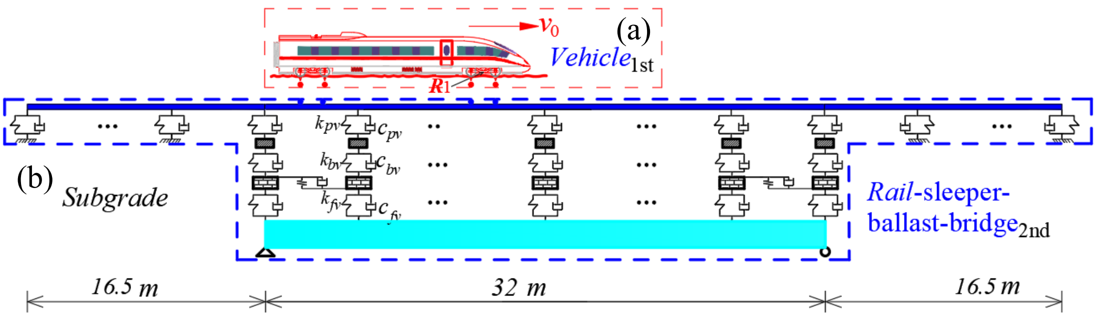

Fig. A1 Two-subsystem model of VRBS. (a) ten-DOF vehicle model and (c) the rail-sleeper-ballast-bridge model.

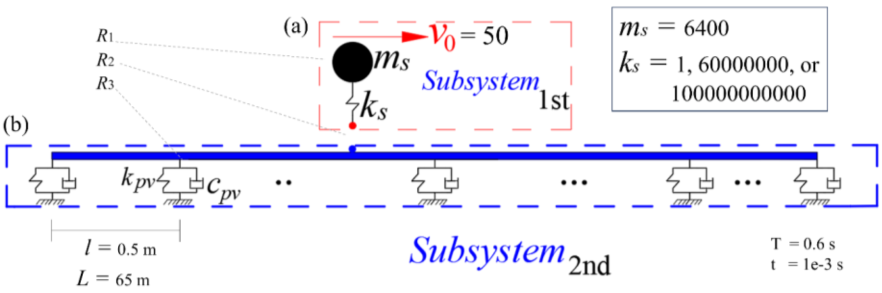

Fig. A2 Two-subsystem model considering (a) the spring-mass subsystem and (b) the continuous beam subsystem.

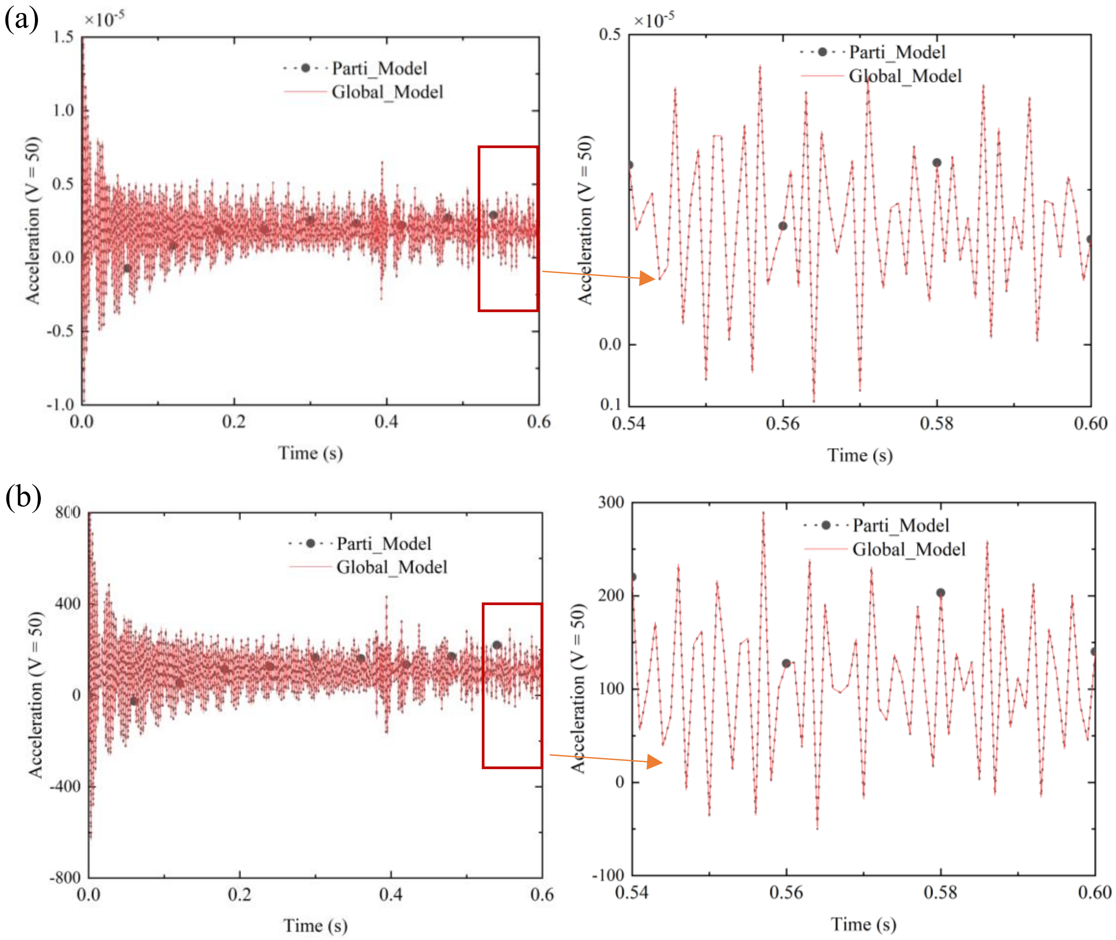

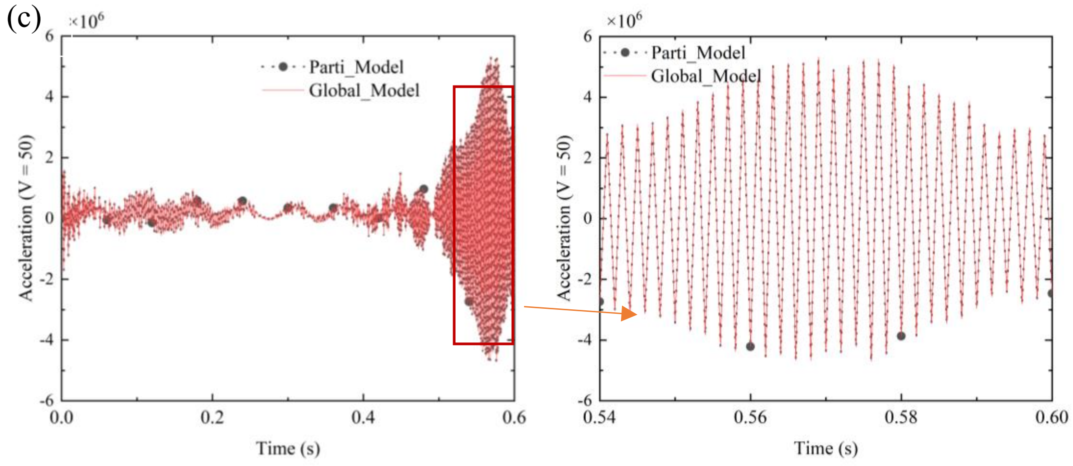

Fig. A3 Accelerations of the partitioned model and global model at R2 when (a) $k_s = 1$, (b) $k_s = 6.0E7$, and (c) $k_s = 1.0E11$.

Appendix D. The parameters for VRBS.

Table 2. System parameters for VRBS.

Parameters	Notation	Unit	Values
Vehicle			
Mass of the car body	m_c	*kg*	3.40E4
Mass of bogie	m_t	*kg*	3.00E3
Mass of wheelset	m_w	*kg*	1.40E3
Mass moment of inertia of car body	*Jc*	$kg.m^2$	2.28E6
Mass moment of inertia of a bogie	*Jt*	$kg.m^2$	2.71E3
Stiffness of the primary suspension system	*Ktz*	*N/m*	8.00E5
Stiffness of the secondary suspension system	*Kpz*	*N/m*	1.10E6
Damping of the primary suspension system	*Ctz*	*N.s/m*	1.60E5
Damping of the secondary suspension system	*Cpz*	*N.s/m*	1.20E4
Half the distance of two wheelsets	*Lt*	*m*	1.2
Half the distance of two bogies	*Lc*	*m*	9
Half-length of car body	*Lv*	*m*	11.8
Vehicle speed	v_0	*m/s*	100
Rail-sleeper-ballast			
Rail mass per meter	m_r	*kg*	60.9
Rail cross-sectional area	A_r	m^2	7.745E-3
Rail bending moment of inertia	Iyr	m^4	3.217E-5
Sleeper mass	m_s	*kg*	237
Ballast mass	m_b	*kg*	1365.2
Young's modulus of rail	E_r	N/m^2	2.06E11
Stiffness between rail and sleeper	*Kpv*	*N/m*	1.56E8
Stiffness between sleeper and ballast	*Kbv*	*N/m*	4.80E8
Stiffness between ballast and bridge	*Kfv*	*N/m*	1.30E8

Damping between rail and sleeper	*Cpv*	*N.s/m*	1.00E5
Damping between sleeper and ballast	*Cbv*	*N.s/m*	1.18E5
Damping between ballast and bridge	*Cfv*	*N.s/m*	6.20E4
Length of rail	*Lr*	*m*	60
Bridge			
Mass per meter	m_{br}	*kg/m*	71913.05
Cross-sectional area	A_{br}	m^2	27.137
Young’s modulus	E_{br}	N/m^2	3.50E10
Poisson ratio			0.167
Bending moment of inertia	I_y	m^4	287.57
Length of bridge	L_{br}	*m*	30

References

[1] D. Krattiger, L. Wu, M. Zacharczuk, M. Buck, R.J. Kuether, M.S. Allen, P. Tiso, M.R.W. Brake, Interface reduction for Hurty/Craig-Bampton substructured models: Review and improvements, Mech. Syst. Signal Process. 114 (2019) 579–603. https://doi.org/10.1016/j.ymssp.2018.05.031.

[2] K. Davis, Computational Methods for Partitioned Simulation Coupling :, (2023).

[3] G. Rozema, A.E.P. Veldman, N.M. Maurits, Quasi-simultaneous coupling methods for partitioned problems in computational hemodynamics, Appl. Numer. Math. 184 (2023) 461–481. https://doi.org/10.1016/j.apnum.2022.11.001.

[4] G. Battiato, C.M. Firrone, T.M. Berruti, B.I. Epureanu, Reduction and coupling of substructures via Gram–Schmidt Interface modes, Comput. Methods Appl. Mech. Eng. 336 (2018) 187–212. https://doi.org/10.1016/j.cma.2018.03.001.

[5] G. Abbiati, V. La Salandra, O.S. Bursi, L. Caracoglia, A composite experimental dynamic substructuring method based on partitioned algorithms and localized Lagrange multipliers, Mech. Syst. Signal Process. 100 (2018) 85–112. https://doi.org/10.1016/j.ymssp.2017.07.020.

[6] C.A. Felippa, K.C. Park, C. Farhat, Partitioned analysis of coupled mechanical systems, Comput. Methods Appl. Mech. Eng. 190 (2001) 3247–3270. https://doi.org/10.1016/S0045-7825(00)00391-1.

[7] K.C. Park, C.A. Felippa, R. Ohayon, Partitioned formulation of internal fluid-structure interaction problems by localized lagrange multipliers, Comput. Methods Appl. Mech. Eng. 190 (2001) 2989–3007. https://doi.org/10.1016/S0045-7825(00)00378-9.

[8] P. Yuan, D. Li, C.S. Cai, G. Xu, Time integration method with high accuracy and efficiency for structural dynamic analysis, J. Eng. Mech. 145 (2019) 4019008.

[9] P. Yuan, D. Li, C.S. Cai, G. XU, A Novel Decoupling Dynamic Method with Third-order Accuracy and Controllable Dissipation, Comput. Struct. 249 (2021).

[10] L. Carassale, P. Silvestri, R. Lengu, P. Mazzaron, Modeling rail-vehicle coupled dynamics by a time-varying substructuring scheme, in: Dyn. Substruct. Vol. 4 Proc. 37th IMAC, A Conf. Expo. Struct. Dyn. 2019, 2020: pp. 167–171.
[11] Q. Zeng, C.D. Stoura, E.G. Dimitrakopoulos, A localized lagrange multipliers approach for the problem of vehicle-bridge-interaction, Eng. Struct. 168 (2018) 82–92. https://doi.org/10.1016/j.engstruct.2018.04.040.
[12] P. Yuan, Y. Dong, R. Feng, D.M. Frangopol, Towards probabilistic seismic performance of vehicle-bridge interaction systems: From stochastic dynamic model to fragility analysis, Earthq. Eng. Struct. Dyn. 52 (2023) 88–110. https://doi.org/10.1002/eqe.3750.
[13] M. Renouf, F. Massi, N. Fillot, A. Saulot, Numerical tribology of a dry contact, Tribol. Int. 44 (2011) 834–844. https://doi.org/10.1016/j.triboint.2011.02.008.
[14] J. Brunetti, W. D'Ambrogio, A. Fregolent, Dynamic coupling of substructures with sliding friction interfaces, Mech. Syst. Signal Process. 141 (2020) 106731. https://doi.org/10.1016/j.ymssp.2020.106731.
[15] W. D'Ambrogio, A. Fregolent, Inverse dynamic substructuring using the direct hybrid assembly in the frequency domain, Mech. Syst. Signal Process. 45 (2014) 360–377. https://doi.org/10.1016/j.ymssp.2013.11.007.
[16] C. uk Ahn, S.M. Kim, D. Il Park, J.G. Kim, Refining characteristic constraint modes of component mode synthesis with residual modal flexibility, Mech. Syst. Signal Process. 178 (2022) 109265. https://doi.org/10.1016/J.YMSSP.2022.109265.
[17] J.A. González, K.C. Park, Three-field partitioned analysis of fluid–structure interaction problems with a consistent interface model, Comput. Methods Appl. Mech. Eng. 414 (2023) 116134. https://doi.org/10.1016/j.cma.2023.116134.
[18] Y.-B. Yang, B.-H. Lin, Vehicle-bridge interaction analysis by dynamic condensation method, J. Struct. Eng. 121 (1995) 1636–1643.
[19] Q. Zeng, C.D. Stoura, E.G. Dimitrakopoulos, A localized lagrange multipliers approach for the problem of vehicle-bridge-interaction, Eng. Struct. 168 (2018) 82–92. https://doi.org/10.1016/J.ENGSTRUCT.2018.04.040.
[20] Q.L. Zhang, A. Vrouwenvelder, J. Wardenier, Numerical simulation of train–bridge interactive dynamics, Comput. Struct. 79 (2001) 1059–1075. https://doi.org/10.1016/S0045-7949(00)00181-4.
[21] Y. Bin Yang, C.H. Chang, J.D. Yau, An element for analysing vehicle-bridge systems considering vehicle's pitching effect, Int. J. Numer. Methods Eng. 46 (1999) 1031–1047. https://doi.org/10.1002/(SICI)1097-0207(19991110)46:7<1031::AID-NME738>3.0.CO;2-V.
[22] Y. Bin Yang, Y.S. Wu, A versatile element for analyzing vehicle–bridge interaction response, Eng. Struct. 23 (2001) 452–469. https://doi.org/10.1016/S0141-0296(00)00065-1.
[23] Y.-B. Yang, J.-D. Yau, Vehicle-bridge interaction element for dynamic analysis, J. Struct. Eng. (1997) 7.
[24] H. Xia, N. Zhang, G. De Roeck, Dynamic analysis of high speed railway bridge under articulated trains, Comput. Struct. 81 (2003) 2467–2478.

https://doi.org/10.1016/S0045-7949(03)00309-2.
[25] N. Zhang, H. Xia, Dynamic analysis of coupled vehicle–bridge system based on inter-system iteration method, Comput. Struct. 114–115 (2013) 26–34. https://doi.org/10.1016/J.COMPSTRUC.2012.10.007.
[26] F. Yang, An iterative solution method for dynamic response of bridge-vehicles systems, Earthq. Eng. Struct. Dyn. 25 (1996) 195–215.
[27] S.G.M. Neves, A.F.M. Azevedo, R. Calçada, A direct method for analyzing the vertical vehicle-structure interaction, Eng. Struct. 34 (2012) 414–420. https://doi.org/10.1016/j.engstruct.2011.10.010.
[28] W. Wang, Y. Zhang, H. Ouyang, An iterative method for solving the dynamic response of railway vehicle-track coupled systems based on prediction of wheel-rail forces, Eng. Struct. 151 (2017) 297–311. https://doi.org/10.1016/J.ENGSTRUCT.2017.08.017.
[29] C. Ge, C.A. Tan, K. Lin, L. Wang, On the efficacy and accuracy of freezing technique for the response analysis of time-varying vehicle-bridge interaction systems, J. Sound Vib. 514 (2021) 116453. https://doi.org/10.1016/j.jsv.2021.116453.
[30] C.D. Stoura, E. Paraskevopoulos, E.G. Dimitrakopoulos, S. Natsiavas, A Dynamic Partitioning Method to solve the vehicle-bridge interaction problem, Comput. Struct. 251 (2021). https://doi.org/10.1016/j.compstruc.2021.106547.
[31] T. Kalaycıoğlu, H.N. Özgüven, FRF decoupling of nonlinear systems, Mech. Syst. Signal Process. 102 (2018) 230–244. https://doi.org/10.1016/j.ymssp.2017.09.029.
[32] A. Prakash, K.D. Hjelmstad, A FETI-based multi-time-step coupling method for Newmark schemes in structural dynamics, Int. J. Numer. Methods Eng. 61 (2004) 2183–2204.
[33] P. Yuan, Y. Dong, High-efficient decoupling method for coupling systems with multiple subdomains and time steps, Mech. Syst. Signal Process. 163 (2022) 108159. https://doi.org/10.1016/J.YMSSP.2021.108159.
[34] S.W.B. Klaassen, M. V. van der Seijs, D. de Klerk, System equivalent model mixing, Mech. Syst. Signal Process. 105 (2018) 90–112. https://doi.org/10.1016/j.ymssp.2017.12.003.
[35] S.N. Voormeeren, D.J. Rixen, A family of substructure decoupling techniques based on a dual assembly approach, Mech. Syst. Signal Process. 27 (2012) 379–396. https://doi.org/10.1016/j.ymssp.2011.07.028.
[36] S. Zhang, H. Devriendt, L. Van Belle, W. Desmet, Substructuring based parametric reduced order modelling for large-scale dynamical systems containing viscoelasticity with application to bonded assemblies, Mech. Syst. Signal Process. 191 (2023). https://doi.org/10.1016/j.ymssp.2023.110192.
[37] S. Krenk, Energy conservation in Newmark based time integration algorithms, Comput. Methods Appl. Mech. Eng. 195 (2006) 6110–6124.
[38] K.-J. Bathe, Finite element procedures, Klaus-Jurgen Bathe, 2006.
[39] P. Yuan, S. Adhikari, Y. Dong, A partitioned combined computational method for multi-scale dynamic systems, Int. J. Numer. Methods Eng. (2023).

https://doi.org/10.1002/nme.7256.

[40] J. Li, K. Yu, X. Li, An identical second-order single step explicit integration algorithm with dissipation control for structural dynamics, Int. J. Numer. Methods Eng. 122 (2021) 1089–1132.

[41] P. Yuan, D. Li, C.S. Cai, G. Xu, An efficient decoupling dynamic algorithm for coupled multi-spring-systems, Comput. Struct. 209 (2018) 44–56.

[42] P. Yuan, Y. Dong, D.M. Frangopol, Reliability assessment of railway bridges under high-speed traffic by considering the track quality and the system randomness, in: Bridg. Safety, Maintenance, Manag. Life-Cycle, Resil. Sustain., Barcelona, Spain, n.d.: p. 108.